

Article

Pore Characteristics and Gas Preservation of the Lower Cambrian Shale in a Strongly Deformed Zone, Northern Chongqing, China

Guangming Meng ¹, Tengfei Li ^{2,*}, Haifeng Gai ² and Xianming Xiao ¹

¹ School of Energy Resources, China University of Geosciences (Beijing), Beijing 100083, China; menggm@email.cugb.edu.cn (G.M.); xmxiao@cugb.edu.cn (X.X.)

² State Key Laboratory of Organic Geochemistry, Guangzhou Institute of Geochemistry, Chinese Academy of Sciences, Guangzhou 510640, China; gaihf@gig.ac.cn

* Correspondence: litengfei@gig.ac.cn

Abstract: The Lower Paleozoic marine shale in southern China has undergone several strong tectonic transformations in an extensive region outside the Sichuan Basin. Although some shale strata underwent strong deformation, they still contain a significant amount of shale gas. The gas preservation mechanism in the strongly deformed shale has become the focus of attention. In this paper, the Lower Cambrian gas-bearing shale samples with a strong deformation taken from an exploration well in northern Chongqing, China, were investigated on their pore types and structure, with the aim to reveal the reason for the gas preservation. The pore types of the Lower Cambrian shale are dominated by microfractures and interparticle (interP) pores occurring mainly between clay minerals and between organic matter (OM) and clay minerals, while pores within OM that can be observed by FE-SEM (field emission-scanning electron microscopy) are rare. The shale has a low porosity, with an average of 1.56%, which is mainly controlled by the clay mineral content. The adsorption experiments of low pressure N₂ (LPNA) and CO₂ (LPCA) indicate that the shale is rich in micropores and small mesopores (<2–3 nm) provided mainly by OM, but mesopores with a size range of 3–50 nm are underdeveloped. The shale, as revealed by LPNA data, has dominant slit-like or plate-like pores and an obvious low-pressure hysteresis (LPH), indicating a low gas diffusion. The deformed shale samples with a removal of OM by oxidation and their isolated kerogen further indicate that the LPH is completely related to OM, without any relationship with minerals, while an undeformed shale sample, taken from another well for a comparison, has no obvious LPH for both of its OM-removed sample and kerogen. Based on a comprehensive analysis of the relative data, it is suggested that the nanopores related to OM and clay minerals in the shale were significantly altered owing to the deformation, with a result of the pores being squeezed into the slit-like shape and converted into micropores. This extraordinary pore structure of the shale formed during the deformation process should be the main preservation mechanism of shale gas.

Keywords: Lower Cambrian shale; tectonic deformation; pore structure; low pressure gas adsorption; low pressure hysteresis; shale gas; preservation mechanism



Citation: Meng, G.; Li, T.; Gai, H.; Xiao, X. Pore Characteristics and Gas Preservation of the Lower Cambrian Shale in a Strongly Deformed Zone, Northern Chongqing, China. *Energies* **2022**, *15*, 2956. <https://doi.org/10.3390/en15082956>

Academic Editor: Reza Rezaee

Received: 23 March 2022

Accepted: 16 April 2022

Published: 18 April 2022

Publisher's Note: MDPI stays neutral with regard to jurisdictional claims in published maps and institutional affiliations.



Copyright: © 2022 by the authors. Licensee MDPI, Basel, Switzerland. This article is an open access article distributed under the terms and conditions of the Creative Commons Attribution (CC BY) license (<https://creativecommons.org/licenses/by/4.0/>).

1. Introduction

As an unconventional natural gas resource, shale gas has been exploited commercially for more than several decades. However, the occurrence and enrichment mechanism of shale gas have still remained unclear since the formation that shale gas plays is very complicated and controlled by a variety of geological and geochemical factors [1–9]. In southern China, the Lower Cambrian and Lower Silurian shales are considered to have great potential [10–13], but currently, only the Lower Silurian shale gas has been exploited commercially [14,15]. The Lower Cambrian shale is distributed more widely and displays greater TOC (total organic carbon) content compared with the Lower Silurian shale [5,16–18], but

its exploration and development for shale gas is not optimistic. The gas content and/or gas-containing properties vary considerably. Some shale gas reservoirs with high gas content are dominated by methane [19–23], while others with low gas content are chiefly composed of nitrogen [24–28], implicating that factors controlling the Lower Cambrian shale gas are more complex. Therefore, it is necessary to deeply study the enrichment and preservation mechanism of Lower Cambrian shale gas, thus reducing the risk of shale gas exploration and development.

The nanopore structure of shales is one of the important factors controlling their gas content [29–32]. The International Union of Pure and Applied Chemistry (IUPAC) classifies shale pore as micropore (<2 nm), mesopore (2–50 nm), and macropore (>50 nm) [33]. The Lower Cambrian shale in southern China generally underwent strong tectonic movements [34,35]. In some shale gas blocks, the shale suffered from severe deformation, leading to the damage of bedding textures or even mylonitization [36]. The storage of shale gas related to strong tectonic reformation had been studied by previous scholars [37–42], but it still remained controversial. For example, Shi et al. [42] investigated the pore structure of the Lower Silurian shale samples from different tectonic locations in the Chongqing area of southern China and found that the pore volumes and specific surface areas decreased with the enhancement of their deformation extent. Zhu et al. [39] found that the Lower Cambrian deformed shale samples from the Upper Yangtze area of southern China had an increase in their micropores and connectivity but a decrease in their porosity. However, Ma et al. [36] pointed out that the strong tectonic deformation led the OM and clay minerals in the shale to form a three-dimensional space-connected pore network, which greatly increased the pore spaces and specific surface areas of the shale matrix. Liang et al. [43] and Li et al. [41], based on the studies of artificially deformed shales and naturally deformed shales, suggested that stress deformation could cause a significant improvement in shale reservoir permeability. Therefore, further research is urgently needed to understand the alteration mechanism of porosity and pore structure and their influences on gas storage, especially gas preservation in strongly deformed shale strata.

The Dabashan tectonic belt in northeastern Chongqing, southern China, had experienced strong tectonic reformations, resulting in a severe deformation of the Lower Cambrian shale strata [19,36,39]. Quite different from the Lower Cambrian shales in other blocks in southern China [24–26], the Lower Cambrian shale in this tectonic belt still retains a high content of shale gas, with methane as the main gas component [19,23,36,44]. In this study, a variety of approaches, such as field emission-scanning electron microscopy observations and low pressure gas (N₂ and CO₂) adsorption experiments were applied to investigate the pore characteristics and the controlling factors of the Lower Cambrian deformed gas-bearing shale in this deformed zone. The major purpose of this study was to reveal the micro-mechanism of methane preservation in the deformed shale.

2. Samples and Experiments

2.1. Samples

The studied Lower Cambrian shale samples were taken from well YC2, which is located at the Dabashan tectonic belt (Figure 1a). The Dabashan tectonic belt is the transition area between the Yangtze plate and the Qinling orogenic belt [45,46]. The regional strata mainly include the Sinian, Cambrian, Ordovician, Middle-Lower Silurian, Permian, Triassic and Middle-Lower Jurassic, missing Devonian, Carboniferous, and Tertiary strata. Multiple phases of tectonic movements resulted in several sedimentary discontinuities, with a serious erosion of the strata. Especially since Yanshanian Period (180–140 Ma), an overlapping thrust structure was formed by strong tectonic compression, with a serious deformation of the strata [46]. Black shales developed widely in the Lower Cambrian Shuijingtuo Formation in this area, with a thickness of 80–150 m [19,47], and it is one of the main targets for shale gas exploration in this area. The Lower Cambrian shale has a current burial depth of less than 3000 m, with a large inclination angle, and was exposed to the earth surface as outcrops in many locations. The geological conditions for shale gas preservation are quite

poor. Unexpectedly, several drilling wells implemented in this area showed a significant amount of gas in the Lower Cambrian shale. The desorbed gas content is averaged at $0.65 \text{ m}^3/\text{t}$ from well CY1 and $1.51 \text{ m}^3/\text{t}$ from well CQ1, with a maximum of $3.64 \text{ m}^3/\text{t}$. The gas is composed of 95.38–98.80% methane, with a minor amount of non-hydrocarbon gases [19,23,44].

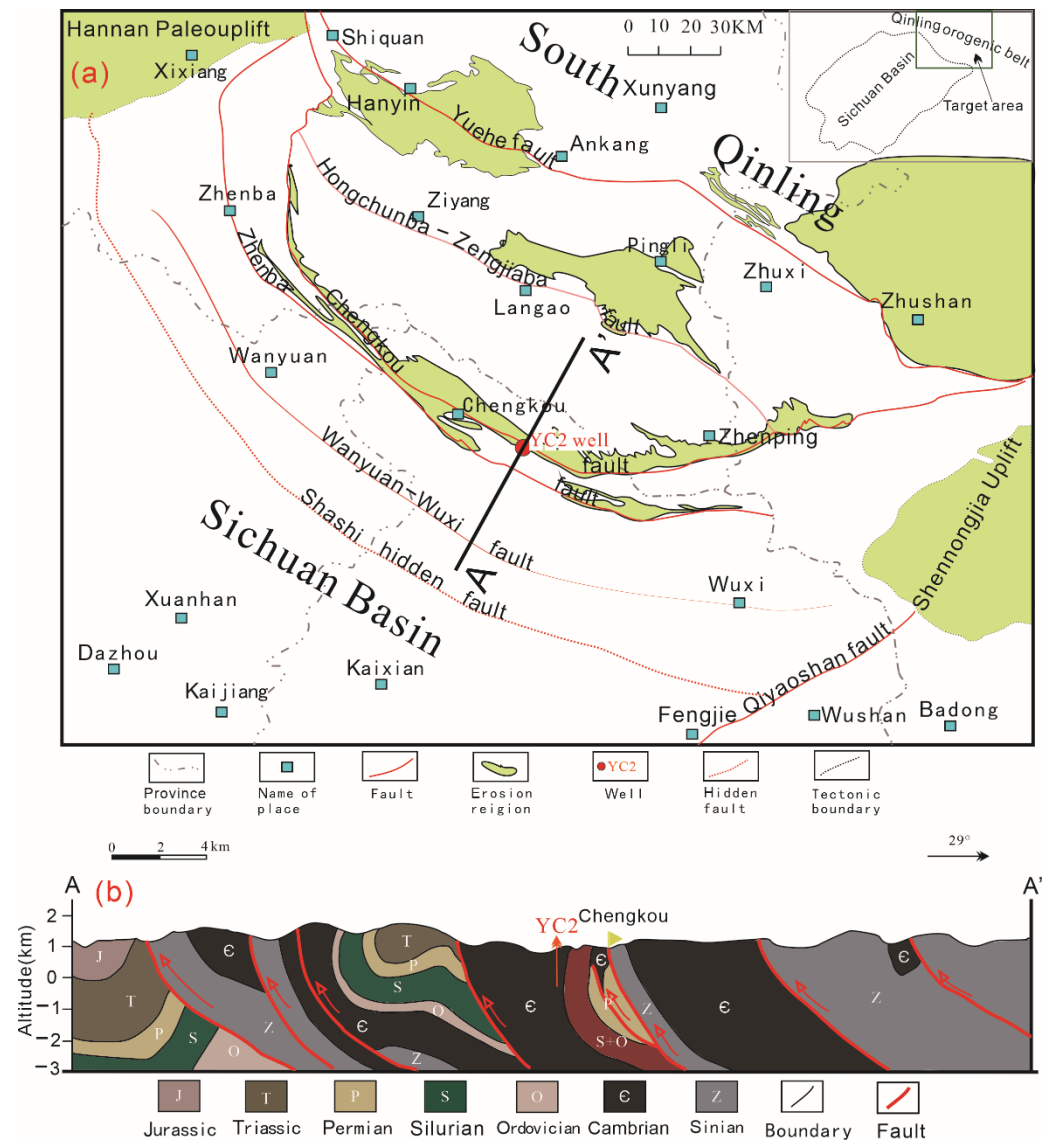


Figure 1. Schematic map to show the geological outline of the Dabashan tectonic belt (a) and a profile to pass through the tectonic belt (b). (a,b) were modified from Yu et al. [19] and Ma et al. [36], respectively.

Well YC2 is close to the Chengkou fault, where tectonic compression is strong. The Lower Cambrian strata have an inclined angle of as high as 35° – 80° (Figure 1b). A total of 10 samples collected from the well were all black shale, with a burial depth of 941.34–1147.68 m. They experienced a heavy deformation, with abundant microfractures filled by irregular veins (Table 1; Figure 2). According to the data from Yu et al. [19], the shale had an average desorbed gas amount of $0.79 \text{ m}^3/\text{t}$, with a maximum of $1.23 \text{ m}^3/\text{t}$, and methane is the main gas component (84.20–99.87%), while N_2 and other non-hydrocarbon gases are approximately less than 10% [48]. For a comparison, a black shale sample of the Lower Cambrian Niutitang Formation from well YC9 in southeastern Chongqing, China, was selected in this study. The area where well YC9 was located has had a relatively stable

geological background [49], and the shale had no obvious deformation, with a complete sedimentary texture. However, its desorbed gas is much less ($0.01\text{--}0.13\text{ m}^3/\text{t}$) and rich in nitrogen ($>90\%$) [49]. The basic geological information and visible features of the 11 samples mentioned above are shown in Table 1.

Table 1. Burial depth and macroscopic characteristics of Lower Cambrian shale samples in this study.

Well/Location	Sample ID	Depth (m)	Lithology	Visible Feature
YC2/Northeastern Chongqing	YC2-1	956.6	black shale	Fragmented and fractured as a whole, without bedding textures, and irregular veins filled in some fractures.
	YC2-2	1004.1	black shale	
	YC2-3	1023.8	black shale	
	YC2-4	1078.8	black shale	
	YC2-5	1086.9	black shale	
	YC2-6	1101.9	black shale	
	YC2-7	1109.7	black shale	
	YC2-8	1115.6	black shale	
	YC2-9	1134.4	black shale	
	YC2-10	1147.6	black shale	
YC9/Southeastern Chongqing	YC9-1	1440.0	black shale	Dense and massive, with clear bedding textures

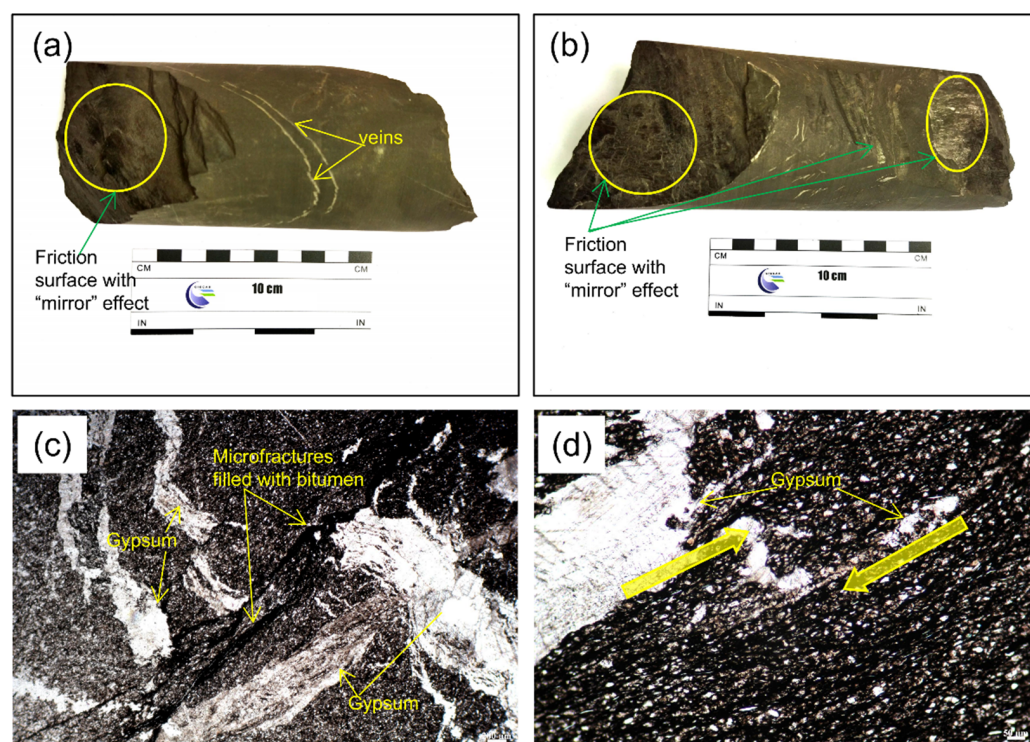


Figure 2. (a) A photograph of the core sample of YC2-3, showing visible friction surfaces with a mirror effect caused by structural friction. (b) A photograph of the core sample of YC2-4, with multiple slippage surfaces and unrecognizable bedding textures. (c) A microscopic photograph of sample YC2-6 (thin section, single polarized light), showing multiple veins composed of gypsum and a fault cutting through the veins that indicates at least one phase of stress action. (d) A photograph of sample YC2-9 (thin section, single polarized light), showing gypsum veins and surrounding mineral matrix with an obvious deformation.

2.2. Experiments

2.2.1. TOC Content Analysis

The samples were crushed into powders of 80 mesh sizes, treated by enough dilute hydrochloric acid to remove carbonate minerals, and then dried at 383.15 K for 12 h. A

LECO CS-200 carbon-sulfur analyzer was applied for the TOC content analysis of the prepared samples, then the peak area of CO₂ generated from combustion of the organic matter and calibrated by carbon steel (TOC = 0.812 ± 0.006%) was calculated, with analytical precision better than 10%.

2.2.2. Solid Bitumen Reflectance Measurement

Although the Lower Cambrian shale samples lack vitrinite, but solid bitumen are abundant, and the solid bitumen reflectance (BRo, %) can be used as an indicator of their maturity. A total of 4 samples were highly polished for sample preparation and reflectance measurements. The used instrument was a 3Y-Leica DMR XP microphotometer, with an objective of 50 × 0.85 in oil immersion and under incident light. The calibration standard samples were YAG-08-57 (Ro = 0.904%) and cubic zirconia (Ro = 3.11%). Large solid bitumen particles with a smooth surface were selected for the measurement in order to reduce the interference from surrounding minerals. More than 50 individual particles were measured for each sample, and their average was deemed as its representative reflectance value.

2.2.3. Mineral Composition Analysis

The mineral composition of the shale samples was analyzed by a Bruker D8 Advance X-ray diffractometer from Germany. The samples (about 2 g for each) were crushed to 200 mesh and dried at 378.15 K for 12 h to remove the moisture and volatile substances. The measured conditions were as follows: a Cu target, an acceleration voltage of 40 KV, a laser diffraction slit width of 1 mm, and a scanning speed of 4°/min. The relative content of minerals was calculated according to their spectral peak areas integration approach with correction of Lorentz Polarization [50,51].

2.2.4. Porosity Measurement

The porosity of the samples (Φ , %) was determined by their skeletal density and apparent density [29], and the calculation formula is as follows:

$$\Phi = (1 - \rho_b / \rho_s) \times 100\% \quad (1)$$

where ρ_b is apparent density (cm³/g), and ρ_s is skeletal density (cm³/g).

The apparent density and skeleton density were measured, respectively, by the wax wrapping method and helium injection method, as suggested by Tian et al. [52].

2.2.5. FE-SEM Observation

The samples were prepared using an argon ion milling instrument (Hitachi High-Tech IM4000), with conditions of an acceleration voltage of 3 kV and a grinding duration of 4 h. The field emission scanning electron microscopy (FE-SEM) applied for the observation was Hitachi S4800. The working voltage was 1–2 kV, and the working distance of the electron gun was 1–8 mm. Both the backscattering (BSE) mode and secondary electron (SE) mode were used in order to identify different minerals and facilitate pore observation.

2.2.6. Kerogen Isolation and OM Oxidation

In order to reveal the organic and inorganic pore structure characteristics of the shale samples, some of them were selected for kerogen isolation and OM oxidation. The method to isolate kerogen from shales suggested by Liu et al. [53] was followed to treat the samples. The purpose for the OM oxidation to the samples is to remove their OM, while leaving their mineral framework. The method recommended by Chen et al. [54] and Gu et al. [55] was followed and is described as below. Shale samples (about 5 g for each) were crushed to 20–40 mesh, dried at 383.15 K for 12 h, and then placed into a muffle furnace to be oxidized at 698.15 K for 24 h. The treated samples were deemed to be OM-free [54].

2.2.7. Low-Pressure Gas Adsorption

The experiments of low-pressure N₂ adsorption (LPNA) and low-pressure CO₂ adsorption (LPCA) were performed with a Micromeritics ASAP 2020 automatic specific surface analyzer. The experimental procedures are as follows. The samples (including original shale, isolated kerogen, and oxidized samples) were crushed to 20–40 mesh and dried at 383.15 K for 12 h. The samples (1.5 g for each) were transferred into the instrument sample tube and degassed for 10 h at 383.15 K under vacuum conditions (<10 mm Hg). The LPNA experiment was performed at the liquid nitrogen temperature (77.4 K) and a relative pressure (P/P_0) range of 0.001–0.995. The LPCA experiment was conducted at the temperature of ice-water mixture (273.15 K) and a relative pressure (P/P_0) range of 0.0001–0.03.

Based on LPNA adsorption branching data, the Barret–Joyner–Hallenda (BJH) model and Brunauer–Emmett–Teller (BET) model were used, respectively, to calculate the pore size distribution (PSD) and specific surface area, with an effective pore size range of 1.7–230 nm. Based on the LPCA data, the micropore volume and specific surface area were calculated, respectively, using density functional theory (DFT) model and the Dubinin–Astakhov (DA) equation [56–58].

3. Results and Discussion

3.1. TOC Content, Mineral Composition, and Maturity

The TOC content of the YC2 well samples ranges from 1.37% to 3.79%, with an average of 2.47% (Table 2), greater than the lowest limit (2%) of the gas-bearing shale with commercial potential [5]. The TOC content varied within a small range, without an obvious relationship with depth, different from the Lower Cambrian shales from other blocks where their TOC increases with depth [59].

Table 2. TOC content, mineralogical composition, and porosity of shale samples.

Sample ID	TOC (%)	Porosity (%)	Mineralogical Composition (%)						
			Quartz	Plagioclase	Illite	Chlorite	Calcite	Dolomite	Pyrite
YC2-1	3.16	1.64	37.1	15.9	25.6	7.2	3.1	8.4	2.6
YC2-2	2.62	1.69	33.7	11.1	29.1	5.9	11.6	6.4	2.2
YC2-3	1.9	1.63	27.6	20.8	29.4	10.4	2.2	3.2	6.4
YC2-4	3.79	1.23	27	23.2	17	0	17.2	14.1	1.5
YC2-5	2.53	1.08	30.2	16.3	19.8	3.9	17.1	10.6	2.2
YC2-6	2.98	1.56	26.8	14	22.5	4.2	24.6	5.4	2.5
YC2-7	1.87	1.34	21.5	14.2	19.3	0	9.2	0	35.8
YC2-8	2.47	1.81	29.9	13.4	35.3	6.5	7.9	4.9	2
YC2-9	2.05	2.15	27.5	17.7	32.6	12.6	5.4	3	1.3
YC2-10	1.37	1.43	28	22.4	26.2	9.8	5.4	6.3	1.9
YC9-1	2.08	2.51	36.5	15.3	37.3	0	0	7.2	3.7

The YC2 well samples are composed of quartz, clay minerals, plagioclase, calcite, pyrite, and a small amount of dolomite (Table 2), and the quartz and clay minerals are their main components. The quartz content ranges from 21.5% to 37.1%, with an average of 28.9%. The clay minerals include illite and chlorite, and their total content ranges from 17.0% to 45.2%, with an average of 31.7%. The carbonate minerals are mainly calcite and dolomite, and their total content ranges from 5.4% to 31.3%, with an average of 16.6%. The samples also contain a certain amount of plagioclase and pyrite, with a content of 11.1–23.2% (an average of 16.9%) and 1.5–35.8% (an average of 5.8%), respectively. Compared with the Lower Silurian shale in typical blocks (e.g., Jiaoshiba block) in southern China [60,61], the YC2 samples have a high content of clay minerals and can be considered to be a clay-rich shale.

Figure 3 shows the correlation between the TOC and four main mineral contents of the YC2 samples. The TOC is positively correlated with quartz, total carbonate minerals, and

dolomite (Figure 3a,b,d), while negatively correlated with the clay minerals (Figure 3c). This is slightly different from the Lower Cambrian shale from well HY1 in northern Guizhou, China, reported by Tian et al. [62]. For their samples, the TOC shows a weak positive correlation with the clay minerals but no obvious correlation with quartz. A positive correlation between TOC and quartz content is generally believed to contain a significant amount of biogenic quartz in shales [60,61,63,64]. The quartz in the YC2 samples may have two origins: biological and detrital, but the latter should be dominant because of the weak positive correlation between the TOC and quartz (Figure 3a).

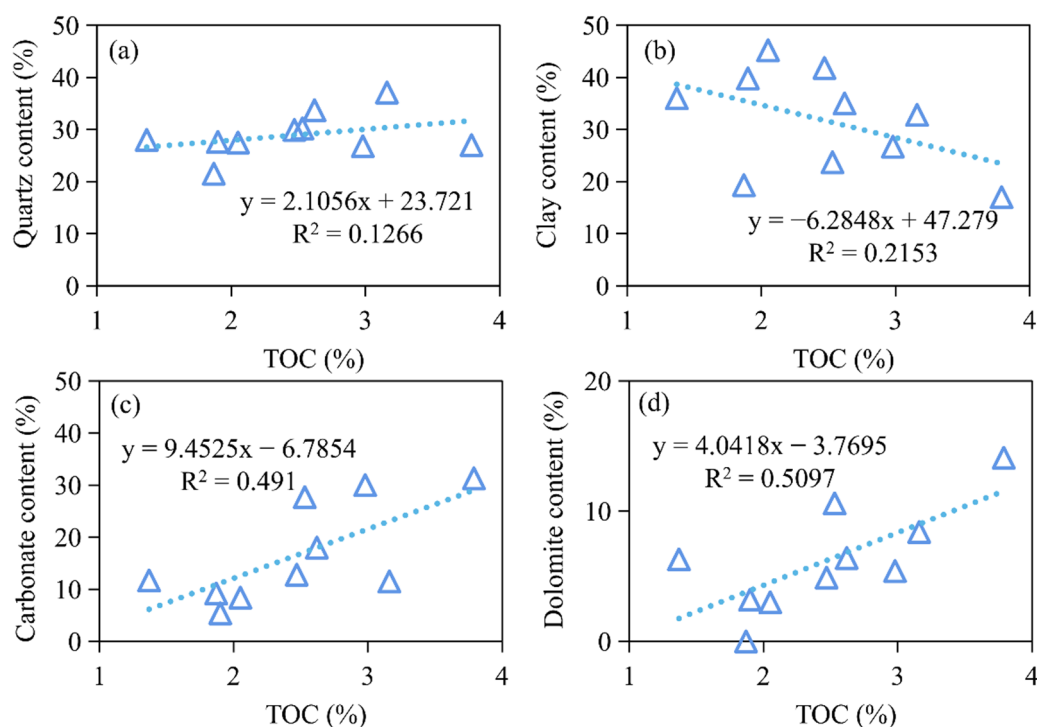


Figure 3. Correlations of TOC with quartz (a), clay (b), total carbonate (c), and dolomite (d) of the YC2 well samples.

Thermal maturity is of great importance for influencing shale porosity, pore structure, and gas-bearing property [65,66]; thus, an accurate evaluation of shale thermal maturity is critical. The maturity of the Lower Cambrian shale in the studied area has been reported in previous studies [36,44,67,68], but with quite different results. For example, the measured BRo value had a range of 3.28–4.25% from Ma et al. [36] and 4.22–5.34% from Cui et al. [67]; the EqRo value (calculated equivalent vitrinite reflectance from bitumen reflectance or other parameters) was between 2.4% and 3.0% from Han et al. [44] and between 3.34% and 3.78% from Wang et al. [68]. The BRo value can be influenced by a series of factors except for maturity, such as the optical anisotropy, size, and internal structure of the measured bitumen particles, as well as the numbers of measured points [69–71], which may be the reason for the great variation in the above results. In order to reduce the influence of the above factors, only large particles, especially band-shaped bitumen without internal structure were selected for the reflectance measurement in this study. The results are shown in Figure 4. Although the BRo ranges of the selected four samples are different, the main peak values are similar, between 3.0% and 3.2%. The averaged BRo values of the four samples are from 3.01% to 3.12%, which gives the EqRo values of 3.10–3.20% by the formula: $EqRo = (BRo + 0.2443)/1.0495$ [69], similar to the maturity of Lower Silurian shales in the Jiaoshiba block of the Sichuan Basin (a commercial shale gas reservoirs in southern China) [72].

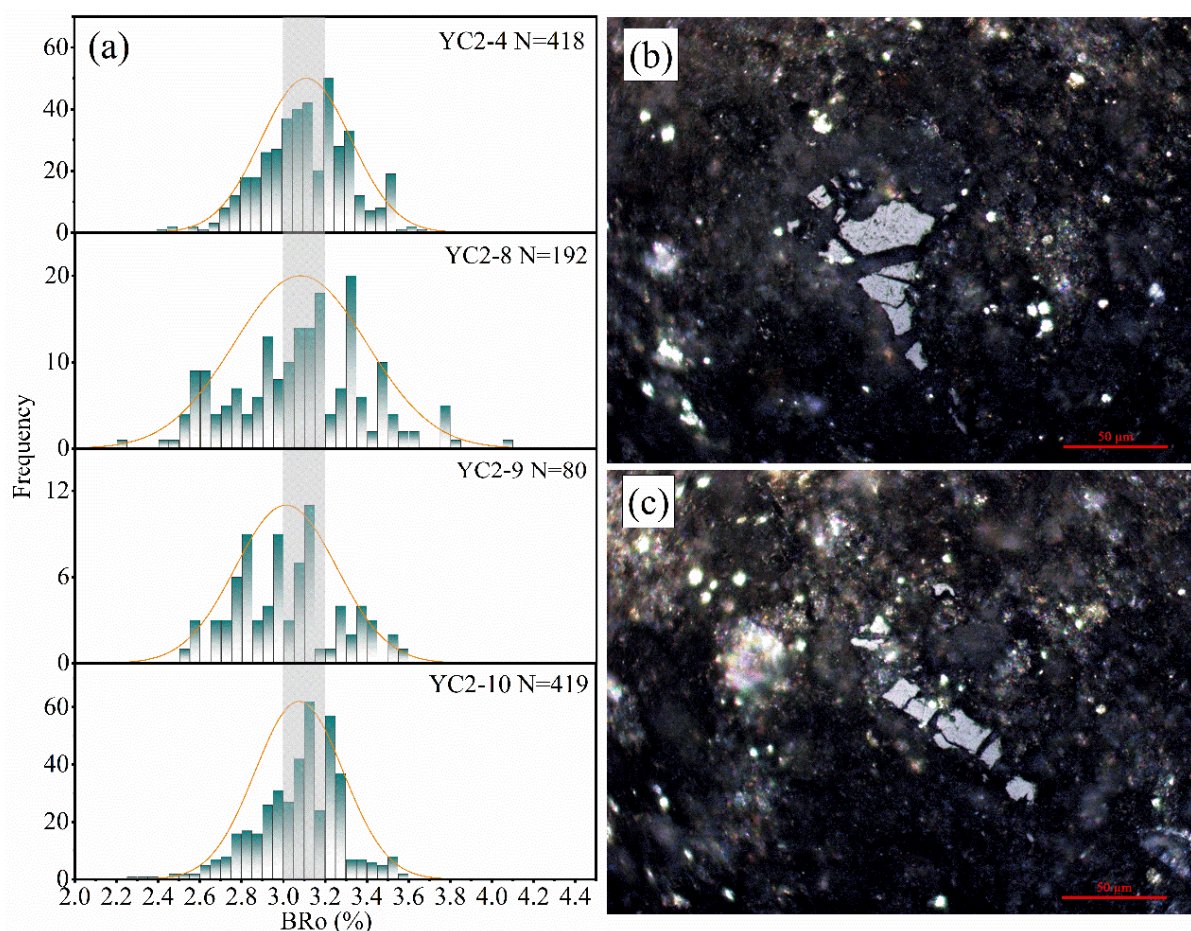


Figure 4. Reflectance distributions of solid bitumen (a) and bitumen micrograph (b,c) of the selected shale samples from well YC2.

Xiao et al. [5] proposed that a maturity with an EqRo value $> 3.5\%$ would be a high risk to shale gas exploration for Lower Paleozoic shales in southern China, which has been verified by pyrolysis experiments and shale gas exploration and development [73–75]. Although the maturity of the YC2 shale samples is quite high, it does not exceed this maturity limit, which is believed to be the basis of the storage of shale gas.

3.2. Pore Types, Porosity and Controlling Factors

The FE-SEM observation revealed that microfractures, interparticle (interP) pores, and intraparticle (intraP) pores occurred widely in the YC2 samples. Some minerals were deformed or fractured to form micro-fractures due to intense extrusion (Figure 5a,b), and some pyrite particles were elongated and oriented (Figure 5a). The interP pores occurred mainly between different particles, especially between clay minerals and between clay minerals and OM. This type of pores is mainly sheet, triangle, and irregular shapes, sizing from a few to hundreds of nanometers (Figure 5c,f). They may be formed by extrusion deformation. The OM in the samples was found mainly in the form of mineral–OM aggregates, with irregular or reticular pores within them (Figure 5d,e), while pores within pore OM particles were rare (Figure 5d,f). IntraP pores developed mainly in carbonate minerals (Figure 5g), with triangular and multilateral shapes, and a size of hundreds of nanometers. Their formation may be related to dissolution. Figure 5h,i shows the pores from sample YC9-1. Compared with the YC2 samples, its microfractures were underdevelopment (Figure 5h), but OM-hosted pores with a diameter of 20–50 nm were widely present (Figure 5i), quite similar to the Lower Cambrian shale from the northern Guizhou, China [62].

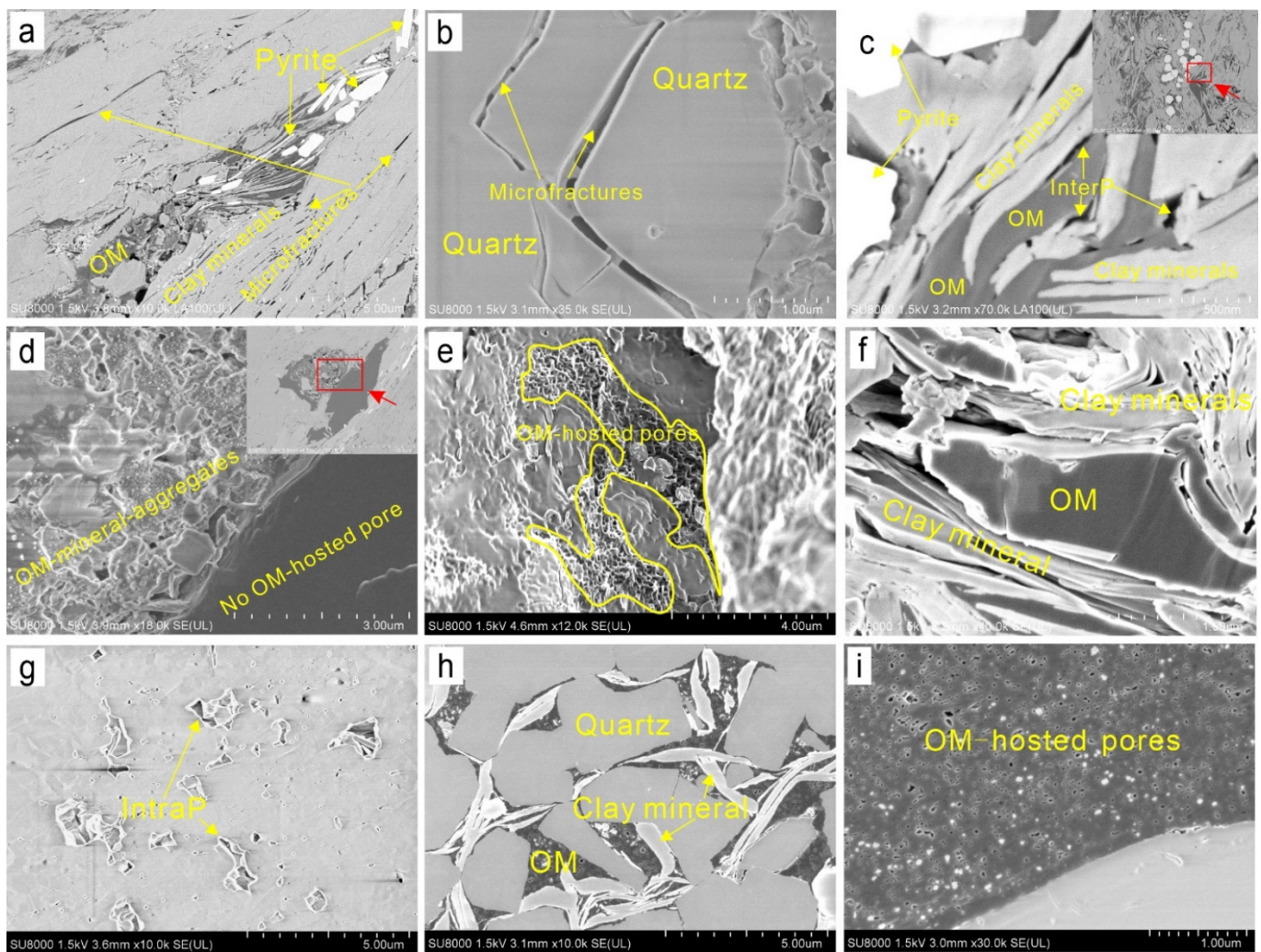


Figure 5. FE-SEM photomicrograph images of the studied shale samples. (a–c): sample YC2-6, BSE model; (d–g): sample YC2-7; (d): BSE model; (e–g): SE model; (h,i): sample YC9-1, SE model. (a): Orientation and deformation of minerals resulted from intense compression, forming interlayer pores and microfractures in clay minerals. (b): Fractures within a single quartz particle. (c): InterP pores between clay and OM, formed by deformation. (d): Irregular pores occurring within OM-mineral aggregates, but rare pores occurring within OM. (e): OM-mineral aggregates with reticular pores. (f): OM between clay minerals, without pores, and interP pores between clay minerals, which may be caused by deformation. (g): Dissolution pores in carbonate minerals. (h,i): OM with a large number of circular and elliptic pores.

The porosity of the YC2 samples is quite small, ranging from 1.08% to 2.15%, with an average of 1.56% (Table 2). The porosity has no obvious correlation with either the TOC or quartz content, but it has a good positive correlation with the clay mineral content ($R^2 = 0.71$) and a weak negative correlation with the carbonate content ($R^2 = 0.31$) (Figure 6). It can be inferred from the results that the porosity of the shale is mainly controlled by its clay minerals.

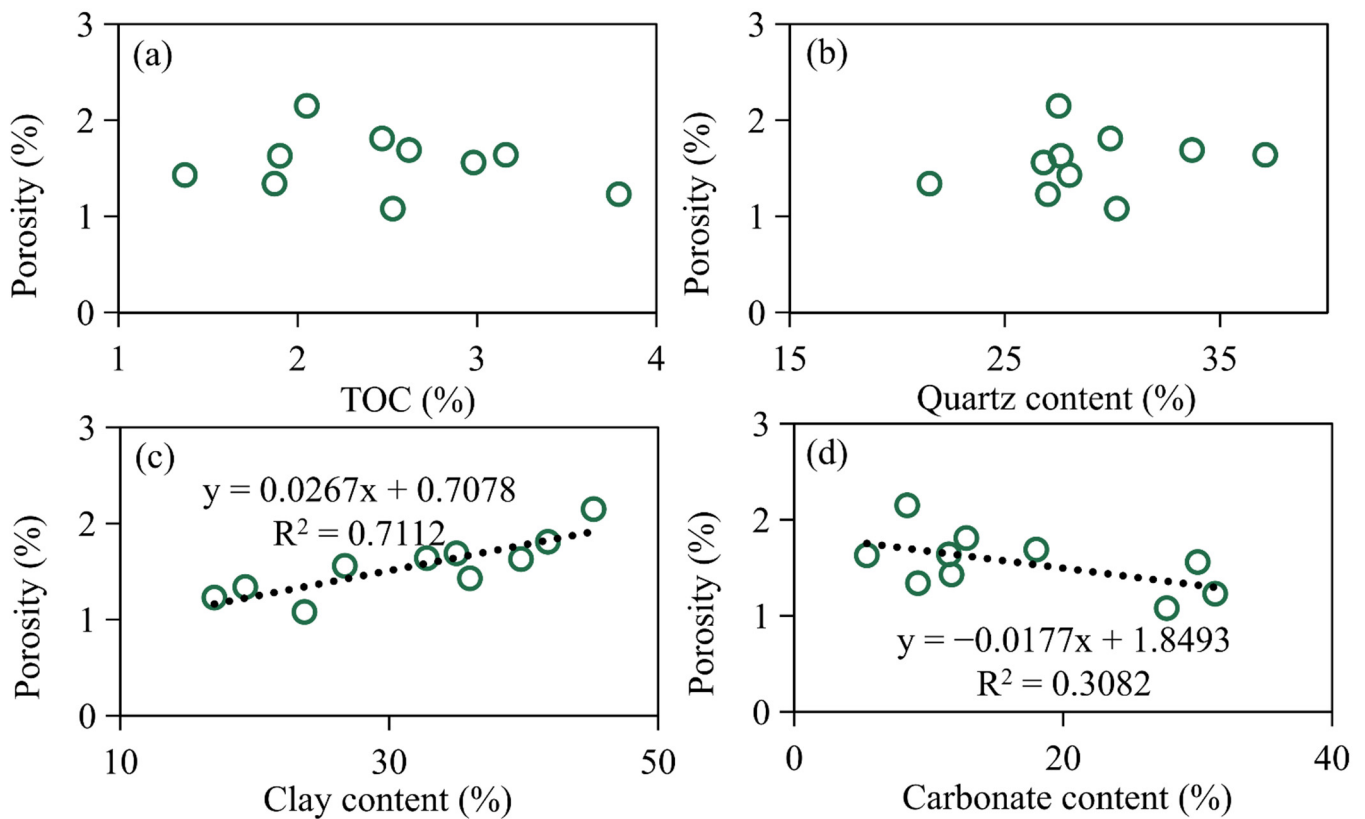


Figure 6. Plots showing relationships of porosity with TOC (a), quartz (b), clay mineral (c), carbonate (d) content for the YC2 samples.

Previous studies have shown that although the porosity of Lower Cambrian shale without obvious deformation in southern China is not greater as a whole, it generally reaches 2–4%, and the TOC content is a dominant controlling factor [12,16,62,76]. For example, Tian et al. [62] reported the porosity of Lower Cambrian shale samples from well HY1 in the northern Guizhou, China, ranged from 2.51% to 4.13%, having a clear positive correlation with their TOC content ($R^2 = 0.77$) but no obvious relationship with their clay minerals. In contrast, the porosity of the YC2 samples is lower, and the clay minerals provide more pore spaces, with a limited contribution from OM pores. The reason may be related to the deformation of clay minerals to form some larger deformed pores and the compaction of larger OM pores into smaller pores. Under the action of intense compressive stress, clay minerals in shales may creep [77], with their original interlayer pores being compacted or deformed to increase spaces due to the existence of unbalanced deformation and distortion [78]; especially, some interP pores protected by brittle minerals (such as pyrite, quartz, etc.) may be enlarged significantly. Although clay minerals may form some larger deformation pores, and some brittle minerals may form tensile microfractures in deformed shales, their total porosity generally shows a decreasing trend [39,79]. Liu et al. [80] also pointed out that the stronger the tectonic stress compression, the lower the porosity of shales. The FE-SEM observation from the YC2 samples and sample YC9-1 are shown in Figure 5, and more data on their pore structure, which is presented in next sections, all support the above interpretation. In addition, the weak negative correlation between porosity and carbonate minerals (Figure 5d) may be related to the cementation of carbonate minerals, which may be another reason for the low porosity of the YC2 samples.

3.3. Pore Structure Characteristics and Controlling Factors

3.3.1. LPNA and LPCA Curves and Pore Size Distribution

According to the gas adsorption mechanism of porous materials, with the increase in relative pressure (P/P_0), gas in pores will be micropore filling, and there will be monolayer and multilayer adsorption on the pore wall, and then capillary condensation up to a high relative pressure [33,81]. LPNA curves of shales can reflect their overall pore characteristics. According to IUPAC, LPNA curves can be divided into four categories based on their hysteresis ring morphology [33]. The LPNA curves of the YC2 samples all are close to type H4 in the IUPAC classification (Figure 7a–e), indicating that their nanopores have silt-like or layered shales. Their adsorption capacity increased rapidly ($P/P_0 < 0.1$) and then slowly ($0.1 < P/P_0 < 0.9$), reflecting the presence of a large number of micropores and a very limited multilayer adsorption, respectively. As $P/P_0 > 0.90$, their adsorption capacity increased rapidly, implicating the capillary condensation occurring in the macropores. Compared with sample YC9-1 (Figure 7f), the YC2 samples present a unique hysteresis ring, although the maximum adsorption quantity between the two well shales is also different—e.g., that of sample YC9YC is significantly greater than that of sample YC2-9 (both have a similar TOC content). Sample YC9-1 has a hysteresis loop as $P/P_0 > 0.5$ and presents a strong “forced closure” phenomenon due to “tensile strength effect” (TSE) [82] in a P/P_0 range of 0.4–0.5, exhibiting a totally reversible adsorption–desorption process as $P/P_0 < 0.4$. However, as for the YC2 samples, their hysteresis rings were not closed, owing to only a slight TSE at the P/P_0 of 0.4–0.5, which resulted in a low pressure hysteresis phenomenon (LPH) [83].

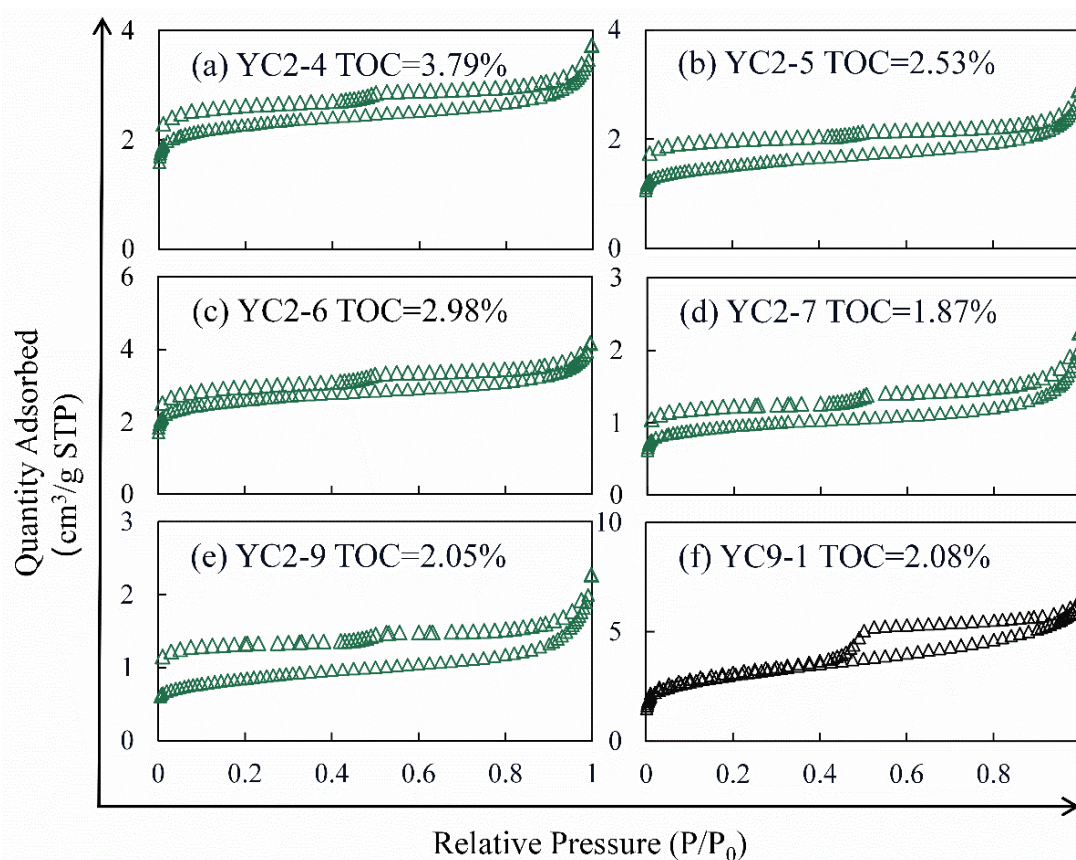


Figure 7. LPNA curves of selected shale samples with different TOC. All samples from well YC2 have a LPH, while sample YC9-1 does not.

The LPCA curves of the samples are shown in Figure 8, and they are similar to the type I isothermal adsorption curve suggested by IUPAC. The slope of the curves has a trend

of gradual decline with increasing pressure, indicating that the growth rate of adsorption capacity decreases. Based on the adsorption capacity at the maximum relative pressure ($P/P_0 \approx 0.03$), the adsorption capacity of the samples to CO_2 can be preliminarily judged. Compared with the samples from well YC2 with a similar TOC content (e.g., YC2-9), the adsorption capacity of sample YC9-1 is also greater.

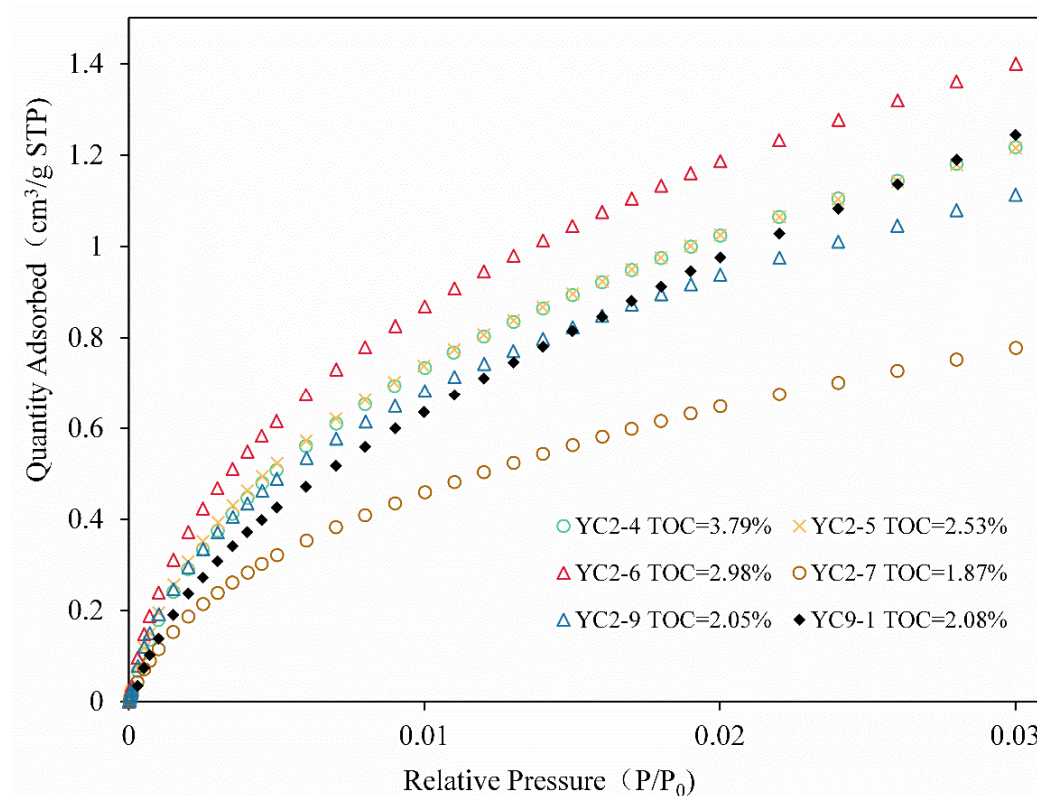


Figure 8. LPCA curves of selected shale samples with different TOC. The adsorption capacity of sample YC9-1 is significantly greater than that of the sample from well YC2 (e.g., YC2-9) with a similar TOC.

As can be seen from the pore size distribution (PSD) curves characterized by the BJH model (Figure 9), the peak value of the YC2 samples is mainly located at about 2 nm, and the peak width is very narrow (1.7–3 nm), indicating that the shale is dominated by micropores and small mesopores. The PSD curve of the sample YC9-1 in the microporous and mesoporous ranges (1.7–50 nm) all are relatively high, without an obvious peak (Figure 9), indicating that both its micropores and mesopores developed well. The PSD (0.35–1.1 nm) curves characterized by DFT model based on LPCA data show that there is no significant difference between the YC2 samples and sample YC9-1 (Figure 10). According to these PSD data, mesopores were greatly reduced in the deformed YC2 shale samples. In a study of the Lower Silurian shale samples with and without deformation from the southeast area of Sichuan Basin, China, Liang et al. [84] also found that tectonic deformation caused an alteration of pore structure in the deformed shale—i.e., from a relatively equal pore distribution, even an advantage of mesopores of the undeformed shale to a pore structure with obvious macropore and micropore advantages of the deformed shale.

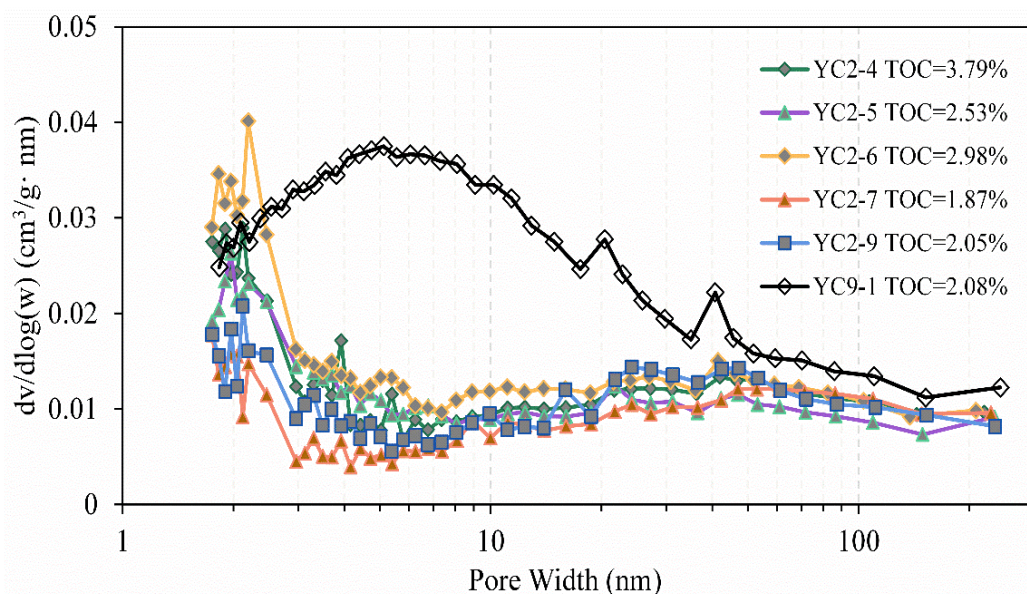


Figure 9. PSD curves of the selected samples with different TOC based on their LPNA data. The peak range is between 1.7 nm and 3 nm for the YC2 samples, while sample YC9-1 has a gentle bulge in a range of 1.7–50 nm, without an obvious peak.

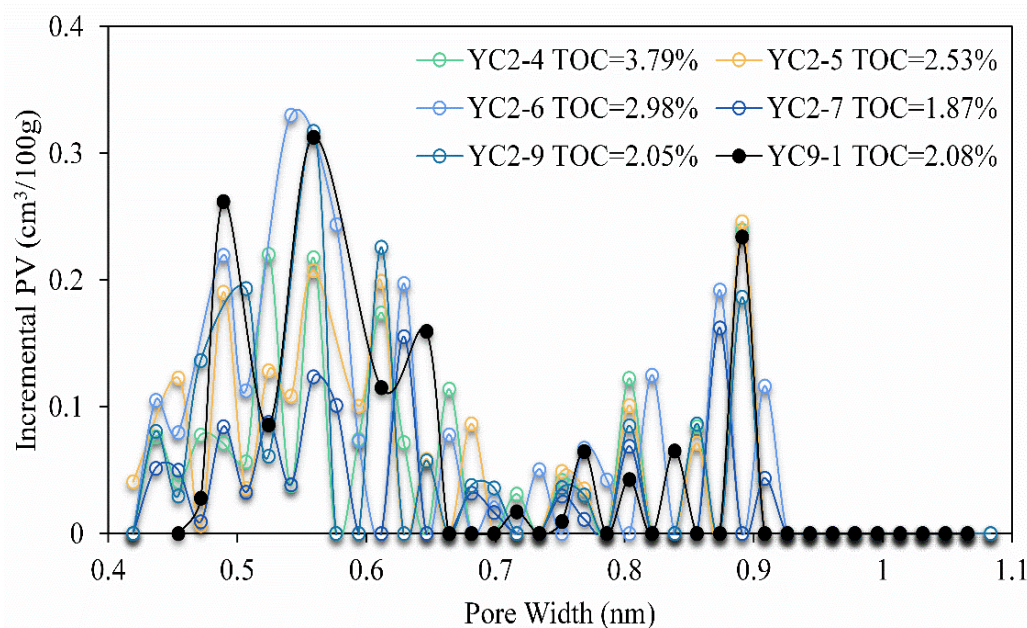


Figure 10. PSD curves of the selected samples with different TOC based on their LPCA data. The YC2 samples and the sample YC9-1 have no significant difference, and both show multi-peaks.

3.3.2. Pore Structure Parameters and Their Controlling Factors

According to the pore structure data of the YC2 samples (Table 3), their V_{BJH} (BJH pore volume), S_{BET} (BET specific surface area), V_{mic} (micropore volume), and S_{mic} (micropore specific surface area) vary in a range of 0.32–0.64 $\text{cm}^3/100\text{g}$, 2.68–9.79 m^2/g , 0.25–0.46 $\text{cm}^3/100\text{g}$, and 6.80–11.96 m^2/g , respectively, with an average of 0.45 $\text{cm}^3/100\text{g}$, 5.55 m^2/g , 0.36 $\text{cm}^3/100\text{g}$, and 9.57 m^2/g , respectively. The S_{mic} and V_{mic} are on average 1.72 and 0.80 times the S_{BET} and V_{BJH} , respectively. The V_{BJH} , S_{BET} , V_{mic} , and S_{mic} values of the sample YC9-1 are 1.00 $\text{cm}^3/100\text{g}$, 10.91 m^2/g , 0.46 $\text{cm}^3/100\text{g}$, and 7.35 m^2/g , respectively. The S_{mic} and V_{mic} are on average 0.62 and 0.46 times of the S_{BET} and V_{BJH} , respectively (Table 3). Compared with the sample YC9-1, the V_{BJH} and S_{BET} of the YC2 samples are much less, while their V_{mic} and S_{mic} are only slightly lower (Table 3), which

further indicates that the YC2 samples are dominated by micropores, while sample YC9-1 has an obvious advantage of mesopores, as presented by their PSD curves in Figure 9.

Table 3. Pore structure parameters of shale samples.

Sample ID	N ₂ Adsorption		CO ₂ Adsorption	
	S _{BET} (m ² /g)	V _{BJH} (cm ³ /100 g)	Smic (m ² /g)	Vmic (cm ³ /100 g)
YC2-1	6.33	0.49	11.96	0.42
YC2-2	3.36	0.42	9.67	0.37
YC2-3	2.68	0.32	7.97	0.30
YC2-4	8.67	0.58	10.94	0.39
YC2-5	5.70	0.45	10.57	0.38
YC2-6	9.79	0.64	11.59	0.46
YC2-7	5.53	0.35	6.80	0.25
YC2-8	4.87	0.44	9.69	0.36
YC2-9	3.11	0.35	9.19	0.36
YC2-10	5.45	0.48	7.35	0.31
YC9-1	10.91	1.00	11.39	0.46

The V_{BJH} and Vmic of the YC2 samples have no significant correlation with their porosity (Figure 11), indicating that their nanopores (<220 nm, the maximum pore size characterized by LPNA in this study) have a limited contribution to their porosity and that their porosity should be provided mainly by macropores with a size of >220 nm.

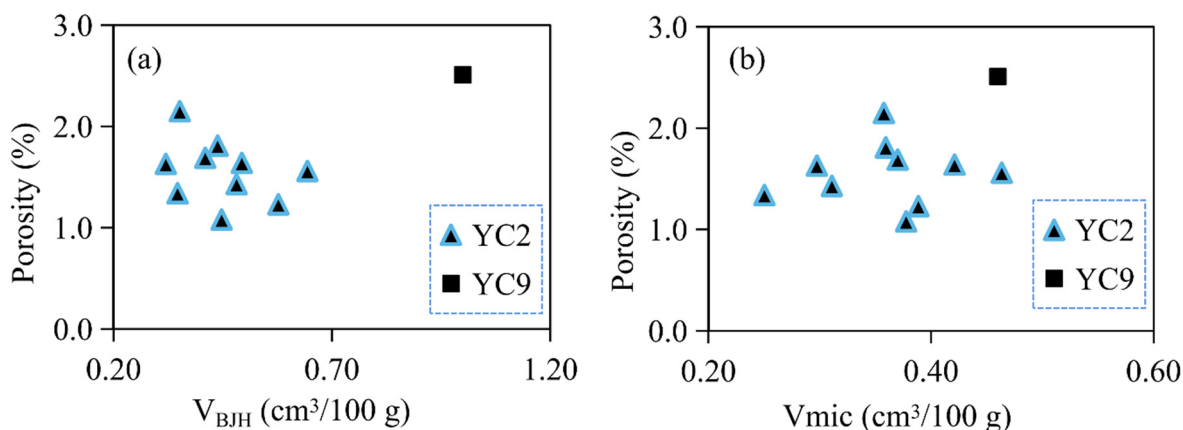


Figure 11. Relationships of porosity with V_{BJH} (a) and Vmic (b) for samples.

Although The TOC content of the YC2 samples has no obvious correlation with porosity, it has clear positive correlations with V_{BJH}, Vmic, S_{BET}, and Smic, and moreover, its correlation with Vmic is better than that with V_{BJH}, and its correlation with Smic is better than that with S_{BET} (Figure 12). Combined with the PSD curves of the samples (Figure 9), it can be believed that the TOC controls not only the micropores but also some of small mesopores (<5–10 nm, the limit of FE-SEM observation) [29,85].

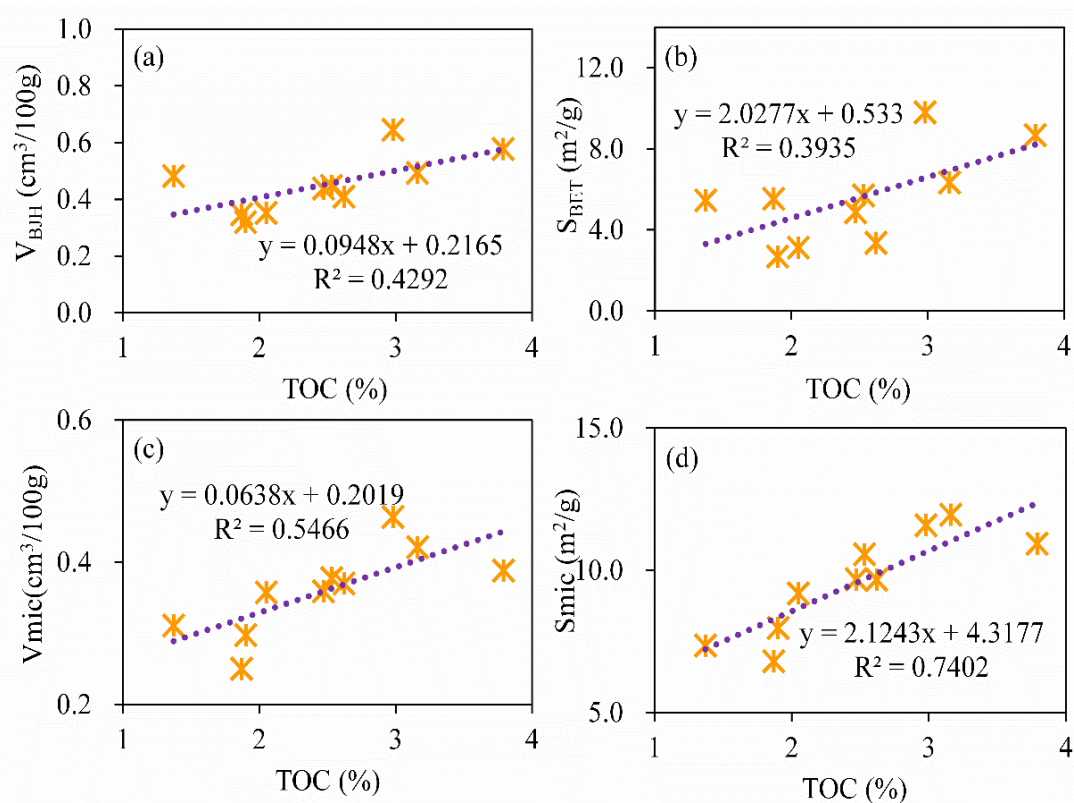


Figure 12. Correlations of TOC with pore structure parameters of the YC2 samples. Subfigures (a–d) show a good correlation between TOC and pore structure parameters. See details in text.

The clay mineral content of the YC2 samples has weak negative correlations with their V_{BJH} and S_{BET} , but no obvious correlation with their V_{mic} and S_{mic} (Figure 13a–d). Considering that the TOC content has a dominant control on pore structure parameters (Figure 12), the pore structure parameters were normalized by the TOC content. The results show that the clay mineral content has no correlation with the V_{BJH}/TOC (ratio of V_{BJH} to TOC) and S_{BET}/TOC (ratio of S_{BET} to TOC), but positive correlations with both the V_{mic}/TOC (ratio of V_{mic} to TOC) and S_{mic}/TOC (ratio of S_{mic} to TOC) (Figure 13e–h), indicating that the clay minerals in the samples contain less mesopores but are rich in micropores. This result is obviously different from previous research on clay minerals. For example, Ji et al. [86,87] documented that micropores in chlorite and illite (both of them are present in the YC2 samples, see Table 2) were underdeveloped, and their pores were dominated by pores with a size of 20–100 nm (mesopores and macropores); Li et al. [88] suggested that 2–50 nm pores in clay minerals provided their main pore volume and specific surface area. Considering that the porosity of the YC2 samples is mainly controlled by the clay minerals (Figure 6c), it can be further deduced that the tectonic deformation resulted in a significant reduction in mesopores in clay minerals, with the formation of some larger deformation macropores and the transformation into micropores.

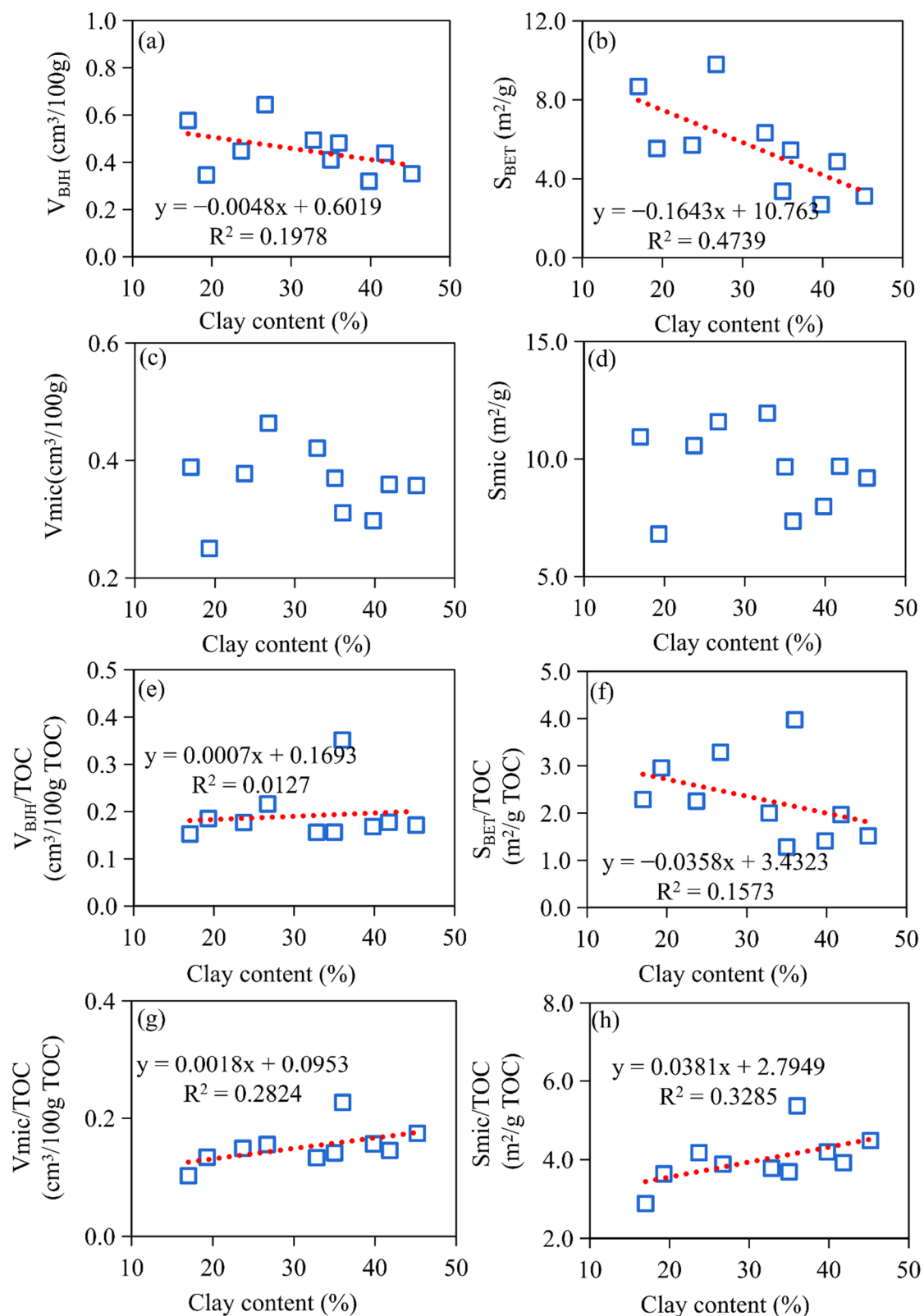


Figure 13. Relationships of clay mineral content with pore structure parameters (a–d), and pore structure parameters/TOC (ratios of pore structure parameters to TOC) (e–h) for the YC2 samples. See details in text.

Similar to the correlation between the quartz content and porosity of the YC2 samples, there is also no obvious relationship of the quartz content with the V_{BJH} and V_{mic}

(Figure 14a,b). Although the carbonate content is positively correlated with the V_{BJH} and V_{mic} (Figure 14c,d), its correlations with $V_{\text{BJH}}/\text{TOC}$ and $V_{\text{mic}}/\text{TOC}$ were also not found (Figure 14e,f). Thus, it can be inferred that the quartz and carbonate minerals have no obvious influence on the pore structure parameters for the YC2 samples. This is consistent with previous studies on the undeformed Lower Cambrian shales in other areas of southern China [62,89].

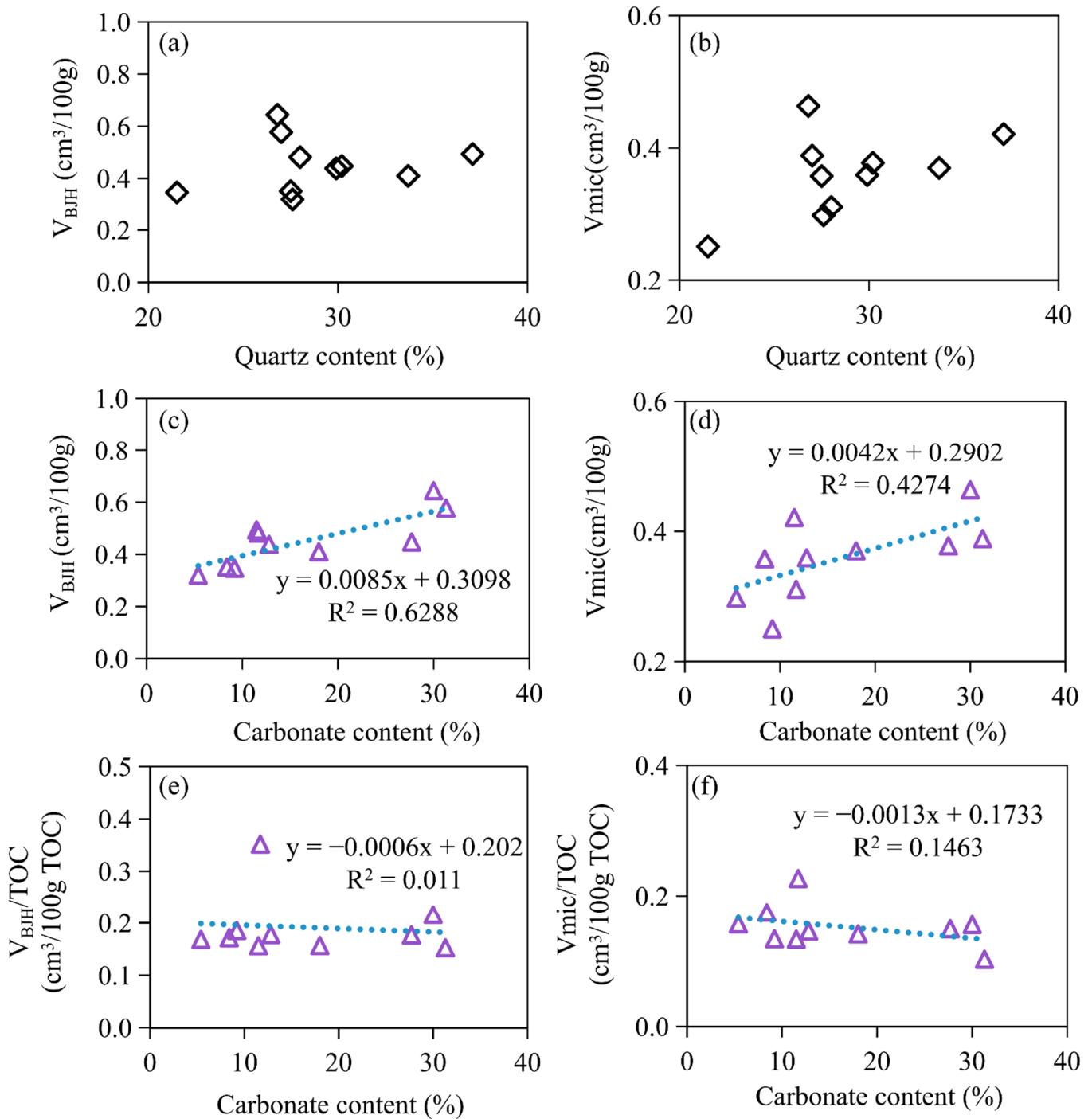


Figure 14. Relationships of quartz and carbonate content with pore structure parameters (a–d), and $V_{\text{BJH}}/\text{TOC}$ (ratio of V_{BJH} to TOC) (e) and $V_{\text{mic}}/\text{TOC}$ (ratio of V_{mic} to TOC) (f) for the YC2 samples. See details in text.

3.4. Mechanism of LPH and Its Significance for Shale Gas Preservation

There are several reports with a LPH record of shales from their LPNA data (e.g., [84,90–92]), but their authors did not give a further explanation of its mechanism. Rouquerol [81] summarized three possible causes for a LPH: adsorption deformation, occurrence of chemical adsorption, and inadequate adsorption balance. Considering that there are not the obvious adsorption deformations and chemical adsorptions in high and over-mature shales [83], the LPH of the YC2 samples should be caused by an imbalance in adsorption, which is most likely related to their special pore structure.

To further reveal the mechanism of LPH of the shale from well YC2, three samples (YC2-6, YC2-7, YC9-1) were selected to obtain their kerogen and OM-oxidized samples (see Section 2.2.6). The mineral composition of the oxidized samples (YC2-6F, YC2-7F, and YC9-1F) remained basically unchanged, compared with their corresponding original shale samples (YC2-6, YC2-7, and YC9-1) (Tables 2 and 4), indicating that the OM in the samples were only removed during the treatment process. Although the TOC content was not measured to the oxidized samples in this study, their OM should have been almost completely removed according to the data from Chen et al. [54]. They reported that the oxidized shale samples have a TOC of <0.1% (using the same method as that in the present study). Thus, it is deemed that oxidized samples can be representative of the minerals in shale samples.

Table 4. TOC and mineral composition of isolated kerogen and OM-oxidized samples.

Sample ID	TOC (%)	Mineral Composition of OM-Oxidized Sample (%)						
		Quartz	Plagioclase	Illite	Chlorite	Calcite	Dolomite	Pyrite
2-6K ¹	47.67	/	/	/	/	/	/	/
2-7K	50.41	/	/	/	/	/	/	/
9-1K	41.23	/	/	/	/	/	/	/
2-6F ²	/	27.9	14.6	23.1	3.5	22.8	6.2	1.9
2-7F	/	20.9	16.8	20.5	0.8	9.8	1.9	29.3
9-1F	/	37.4	14.6	36.3	0	0	9.7	2.0

¹ YC2-6k, YC2-7K and YC9-1K are kerogen samples, respectively, from YC2-6, YC2-7, and YC9-1; ² YC2-6F, YC2-7F, and YC9-1F are OM-oxidized samples, respectively, from YC2-6, YC2-7, and YC9-1; “/” means no data.

LPNA experiments were performed on the kerogen and OM-oxidized samples. According to the adsorption–desorption curves, the OM-oxidized samples (YC2-6F, YC2-7F, YC9-1F) became very similar—without a LPH, but with a hysteresis loop in the high pressure section ($P/P_0 > 0.5$)—while the two kerogens (YC2-6K and YC2-7K) show an obvious LPH, but the kerogen YC9-1K does not (Figure 15). As presented in Figure 7 for their original shale samples, both the YC2-5 and YC2-6 have a LPH (Figure 7c,d), while YC9-1 does not (Figure 7f). Therefore, it can be believed that the LPH of the YC2 samples should be caused by their OM with a pore structure having been altered during strong deformation.

In addition, the adsorption equilibrium duration of those samples seems to depend on whether there is a LPH (Figure 16). As P/P_0 is less than 0.1, the adsorption equilibrium duration of the samples with a LPH (YC2-6, YC2-6K, YC2-7, YC2-7K) is much greater than those without a LPH (YC2-6F, YC2-7F, YC9-1, YC9-1K, YC9-1F), and the data of the three OM-oxidized samples (YC2-6F, YC2-7F, YC9-1F) became overlapped, indicating the minerals in the shales have a very similar adsorption behavior. For a specific shale sample, the equilibrium duration order is kerogen > original shale > OM-oxidized sample.

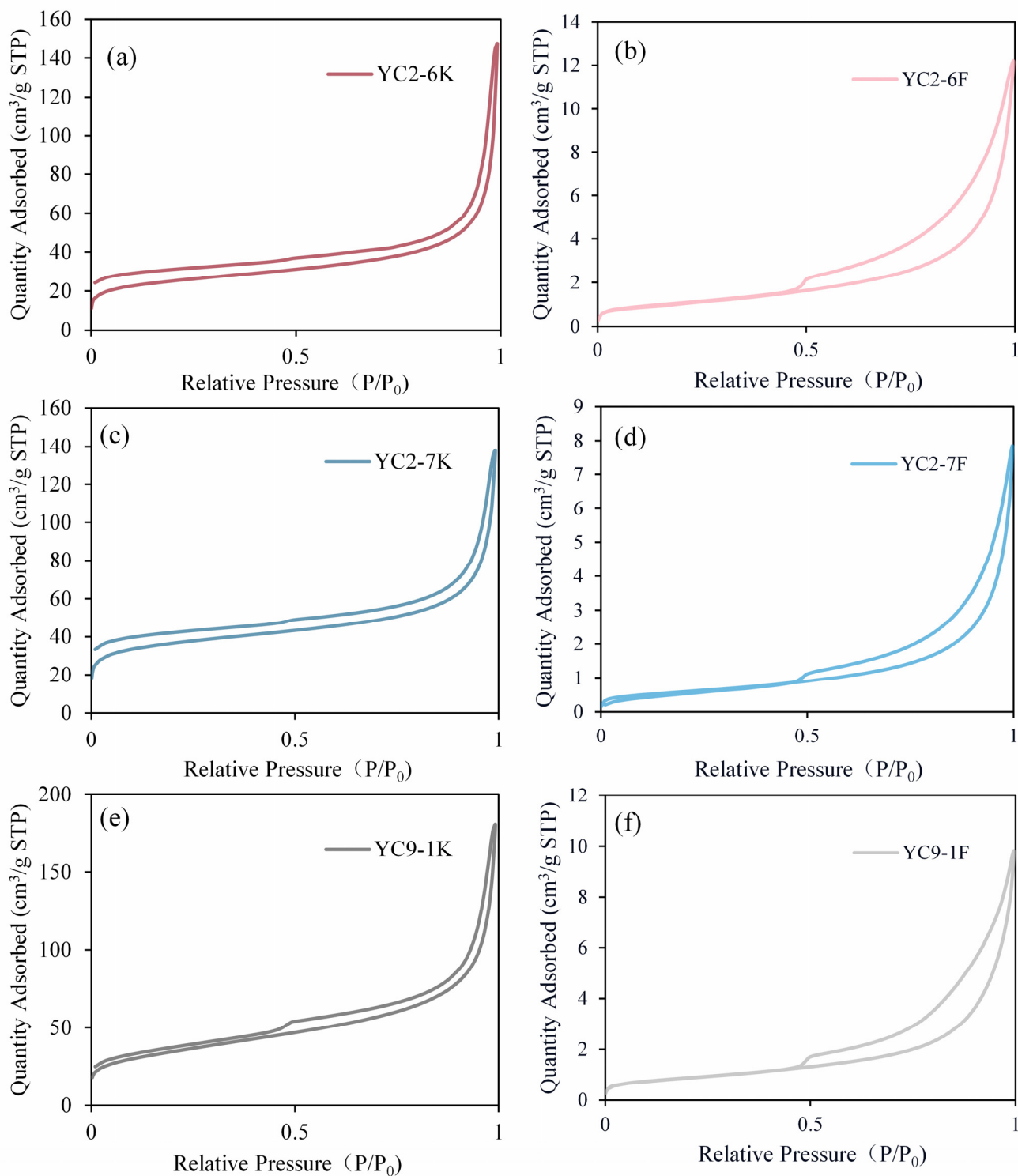


Figure 15. LPNA curves for isolated kerogen (a,c,e) and OM-oxidized (b,d,f) samples. See details in text.

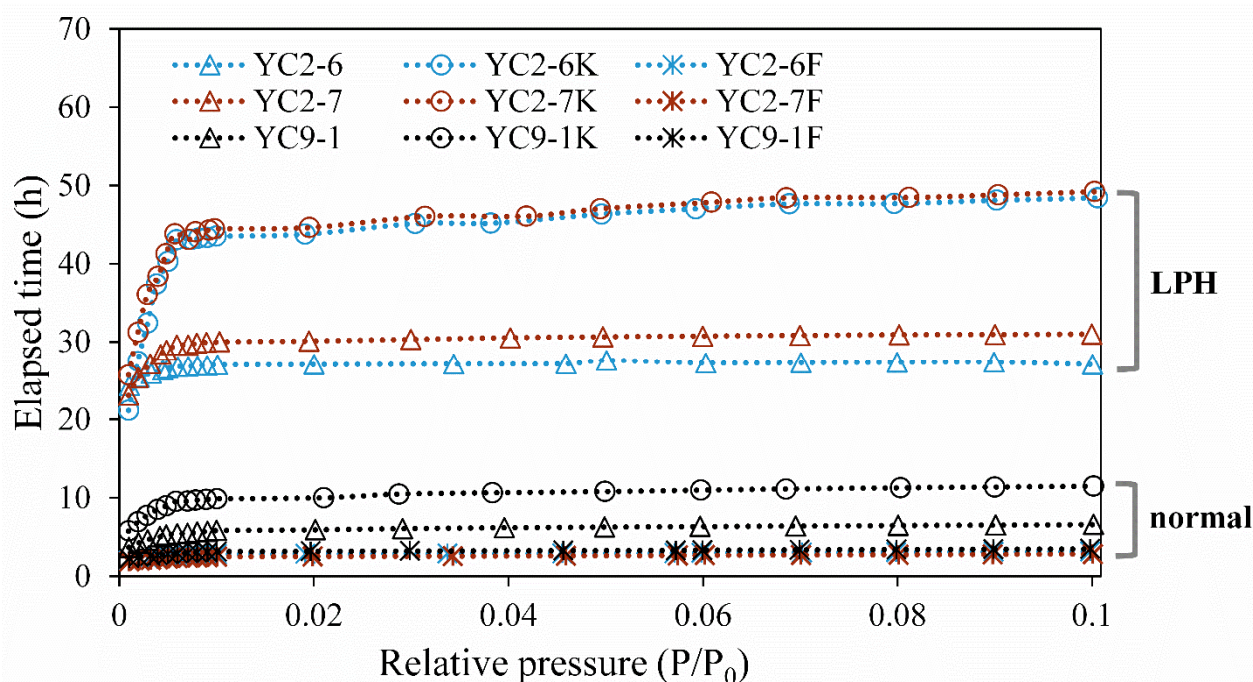


Figure 16. Adsorption equilibrium duration of different types of samples with or without a LPH. See details in text.

Gas diffusion in the shale nanopore system is mainly characterized by Fick diffusion, Knudsen diffusion, and surface diffusion [93–95]. As a shale is dominated by micropores, its gas diffusion is dominated by surface diffusion, owing to the influence of surface adsorption potentials, with a diffusion coefficient to be closely related to pore diameter and morphology [95–97]. If the diffusion is insufficient in a finite time, the resulting LPNA curve will show a LPH [83]. Therefore, the LPH of a shale indicates that its pore structure is characterized by low diffusion.

The leakage process of shale gas mainly includes desorption and diffusion [97]. As the pore diameter of a shale becomes smaller, its gas adsorption potential energy will increase, meaning that its gas desorption will overcome a greater resistance. As discussed in above sections, the YC2 samples are mainly characterized by micropores and small mesopores, with undeveloped mesopores, and their pores, such as OM-hosted pores and clay-hosted pores may be flattened by extrusion and/or compaction to have silt-like or layered shapes. This unique pore structure is obviously not conducive to gas loss and would play an important role in the preservation of shale gas. On the other hand, the Lower Cambrian shale gas in southern China is usually rich in N_2 [25–27]. A high content of N_2 in shale strata is generally believed to be sourced from the thermal decomposition of their organic matter and NH_4^+ -rich minerals, and/or from the atmospheric N_2 infiltration [24,25,27,74]. The thermal decomposition-derived N_2 occurs mainly at a very high maturity stage, e.g., $EqRo > 3.5\%$ according to Gai et al. [74], while the YC2 samples have an $EqRo$ of 3.1–3.2% (see Section 2.2), within the maturity range of methane generation and preservation [5,75]. In addition, the Lower Cambrian shale at well YC2 is currently shallowly buried and has a high dip angle, which is suitable for the infiltration of atmospheric N_2 . However, the shale gas contains only a minor amount of N_2 . This further suggests that the unique pore structure of the shale has prevented N_2 from entering its nanopore system and that the reserved methane has been preserved. These two aspects are believed to be the basic reasons for the preservation of the Lower Cambrian shale gas at well YC2. However, it should be pointed out that whether this mechanism has a general significance for shale gas exploration and development in strongly deformed shale strata in southern China needs to be verified by more cases.

4. Conclusions

In this research, the pore characteristics and pore structure and the controlling factors of the Lower Cambrian gas-bearing shale samples with strong tectonic deformation taken from the YC2 well in southern China were investigated, and the main conclusions have been drawn as follows:

- (1) The pore types of the shale are microfractures—interP pores occurring mainly between clay minerals and OM-clay mineral composite pores within their aggregates—and all of them were formed or obviously affected by extrusion deformation. The porosity of the shale is low, and it is mainly contributed by macropores with a size of >220 nm and controlled by clay mineral content.
- (2) The pore structure of the shale is characterized by predominant micropores and 2–3 nm mesopores that are mainly contributed by organic matter and an underdevelopment of 3–50 nm mesopores, with dominant pores being a slit-like or layered shape.
- (3) The alteration of OM and clay mineral-related pores by strong deformation appears to be the main mechanism for the formation of the unique pore structure of the shale. This results in an obvious low pressure hysteresis of the LPNA curve caused by low gas diffusion, which is the main reason for the preservation of shale gas. This explanation gives a new significance to the LPH phenomenon, that is, it indicates a lower gas diffusion rate. This study provides new enlightenment for the preservation mechanism of shale gas under a background of complex structure.

Author Contributions: Conceptualization, X.X. and G.M.; methodology, H.G. and T.L.; software, G.M.; validation, X.X. and T.L.; formal analysis, G.M.; investigation, G.M.; resources, X.X. and T.L.; data curation, G.M.; writing—original draft preparation, G.M.; writing—review and editing, X.X.; visualization, G.M.; supervision, X.X.; project administration, X.X.; funding acquisition, X.X. All authors have read and agreed to the published version of the manuscript.

Funding: This research was funded by the National Natural Science Foundation of China, grant numbers 42030804, 42103049, and U19B6003-03-01.

Institutional Review Board Statement: Not applicable.

Informed Consent Statement: Not applicable.

Data Availability Statement: Not applicable.

Conflicts of Interest: The authors declare no conflict of interest.

References

1. Curtis, J.B. Fractured Shale-Gas Systems. *AAPG Bull.* **2002**, *86*, 1921–1938.
2. Ross, D.J.K.; Bustin, R.M. Characterizing the shale gas resource potential of Devonian–Mississippian strata in the Western Canada sedimentary basin: Application of an integrated formation evaluation. *AAPG Bull.* **2008**, *92*, 87–125. [[CrossRef](#)]
3. Ross, D.J.K.; Marc Bustin, R. The importance of shale composition and pore structure upon gas storage potential of shale gas reservoirs. *Mar. Pet. Geol.* **2009**, *26*, 916–927. [[CrossRef](#)]
4. Nie, H.; Tang, X.; Bian, R. Controlling factors for shale gas accumulation and prediction of potential development area in shale gas reservoir of South China. *Acta Pet. Sin.* **2009**, *30*, 484–491. (In Chinese with English abstract)
5. Xiao, X.; Wei, Q.; Gai, H.; Li, T.; Wang, M.; Pan, L.; Chen, J.; Tian, H. Main controlling factors and enrichment area evaluation of shale gas of the Lower Paleozoic marine strata in south China. *Pet. Sci.* **2015**, *12*, 573–586. [[CrossRef](#)]
6. Jia, C.; Pang, X.; Song, Y. The mechanism of unconventional hydrocarbon formation: Hydrocarbon self-sealing and intermolecular forces. *Pet. Explor. Dev.* **2021**, *48*, 507–526. [[CrossRef](#)]
7. Guo, T. Key geological issues and main controls on accumulation and enrichment of Chinese shale gas. *Pet. Explor. Dev.* **2016**, *43*, 349–359. [[CrossRef](#)]
8. Zou, X.; Li, X.; Zhang, J.; Li, H.; Guo, M.; Zhao, P. Characteristics of Pore Structure and Gas Content of the Lower Paleozoic Shale from the Upper Yangtze Plate, South China. *Energies* **2021**, *14*, 7603. [[CrossRef](#)]
9. Gao, P.; Xiao, X.; Hu, D.; Liu, R.; Cai, Y.; Yuan, T.; Meng, G. Water Distribution in the Ultra-Deep Shale of the Wufeng-Longmaxi Formations from the Sichuan Basin. *Energies* **2022**, *15*, 2215. [[CrossRef](#)]
10. Zhang, J.; Shi, M.; Wang, D.; Tong, Z.; Hou, X.; Niu, J.; Li, X.; Li, Z.; Zhang, P.; Huang, Y. Fields and directions for shale gas exploration in China. *Nat. Gas Ind.* **2021**, *41*, 69–80. (In Chinese with English abstract) [[CrossRef](#)]

11. Liang, D.; Guo, T.; Chen, J.; Bian, L.; Zhe, Z. Some Progresses on Studies of Hydrocarbon Generation and Accumulation in Marine Sedimentary Regions, Southern China (Part 1): Distribution of Four Suits of Regional Marine Source Rocks. *Mar. Orig. Pet. Geol.* **2008**, *13*, 1–16. (In Chinese with English abstract)
12. Zou, C.; Dong, D.; Wang, S.; Li, J.; Li, X.; Wang, Y.; Li, D.; Cheng, K. Geological characteristics and resource potential of shale gas in China. *Pet. Explor. Dev.* **2010**, *37*, 641–653. [[CrossRef](#)]
13. Zhao, W.; Li, J.; Yang, T.; Wang, S.; Huang, J. Geological difference and its significance of marine shale gases in South China. *Pet. Explor. Dev.* **2016**, *43*, 547–559. [[CrossRef](#)]
14. Guo, T. Discovery and characteristics of the Fuling shale gas field and its enlightenment and thinking. *Earth Sci. Front.* **2016**, *23*, 29–43. (In Chinese with English abstract)
15. Dai, J.D.D.; Ni, Y.; Hong, F.; Zhang, S.; Zhang, Y.; Ding, L. Some essential geological and geochemical issues about shale gas research in China. *Nat. Gas Geosci.* **2020**, *31*, 745–760. (In Chinese with English abstract)
16. Yan, J.; Men, Y.; Sun, Y.; Yu, Q.; Liu, W.; Zhang, H.; Liu, J.; Kang, J.; Zhang, S.; Bai, H.; et al. Geochemical and geological characteristics of the Lower Cambrian shales in the middle–upper Yangtze area of South China and their implication for the shale gas exploration. *Mar. Pet. Geol.* **2016**, *70*, 1–13. [[CrossRef](#)]
17. Hu, M.; Deng, Q.; Hu, Z. Shale gas accumulation conditions of the Lower Cambrian Niutitang Formation in Upper Yangtze region. *Oil Gas Geol.* **2014**, *35*, 272–279. (In Chinese with English abstract)
18. Wang, P.; Jiang, Z.; Han, B.; Lv, P.; Li, T. Reservoir geological parameters for efficient exploration and development of Lower Cambrian Niutitang Formation shale gas in South China. *Acta Pet. Sin.* **2018**, *39*, 152–162.
19. Yu, C.; Zeng, C.; Zhou, X.; Nie, H.-k.; Yu, Z. Tectonic preservation unit division and zoning evaluation of shale gas in the Lower Cambrian of Dabashan thrust belt. *Nat. Gas Geosci.* **2018**, *29*, 853–865. (In Chinese with English abstract)
20. Dong, D.; Caineng, Z.; Hua, Y.; Yuman, W.; Xinjing, L.; Gengsheng, C.; Shiqian, W.; Zonggang, L.; Yongbin, H. Progress and prospects of shale gas exploration and development in China. *Acta Pet. Sin.* **2012**, *33* (Suppl. S1), 107–114. (In Chinese with English abstract)
21. Chen, X.; Wang, C.; Lliu, A.; Luo, S.; Li, H.; Wei, K. The discovery of the shale gas in the Cambrian Shuijingtuo Formation of Yichang area, Hubei Province. *Geol. China* **2017**, *44*, 188–189. (In Chinese with English abstract)
22. Chen, X.; Bao, S.; Zhai, G.; Zhou, Z.; Tong, C.; Wang, C. The discovery of shale gas within Lower Cambrian marine facies at Shan Nandi-1 well on the margin of Hannan palaeouplift. *Geol. China* **2018**, *45*, 412–413. (In Chinese with English abstract)
23. Han, H.; Li, D.; Ma, Y.; Lijun, C.; Qi, L.; Wang, Q.; Zhong, N. The origin of marine shale gas in the northeastern Sichuan Basin, China: implications from chemical composition and stable carbon isotope of desorbed gas. *Acta Pet. Sin.* **2013**, *34*, 453–459. (In Chinese with English abstract)
24. Liu, Y.; Zhang, J.; Ren, J.; Liu, Z.; Huang, H.; Tang, X. Stable isotope geochemistry of the nitrogen-rich gas from lower Cambrian shale in the Yangtze Gorges area, South China. *Mar. Pet. Geol.* **2016**, *77*, 693–702. [[CrossRef](#)]
25. Jiao, W.; Wang, S.; Cheng, L.; Luo, Q.; Fang, G. The reason of high nitrogen content and low hydrocarbon content of shales gas from the Lower Cambrian Niutitang Formation in southeast Chongqing. *Nat. Gas Geosci.* **2017**, *28*, 1882–1890. (In Chinese with English abstract)
26. Wu, Y.; Gong, D.; Li, T.; Wang, X.; Tian, H. Distribution characteristics of nitrogen-bearing shale gas and prospective areas for exploration in the Niutitang Formation in the Qianzhong uplift and adjacent areas. *Geochimica* **2019**, *48*, 613–623. (In Chinese with English abstract)
27. Wang, X.; Jiang, Z.; Zhang, K.; Wen, M.; Xue, Z.; Wu, W.; Huang, Y.; Wang, Q.; Liu, X.; Liu, T.; et al. Analysis of Gas Composition and Nitrogen Sources of Shale Gas Reservoir under Strong Tectonic Events: Evidence from the Complex Tectonic Area in the Yangtze Plate. *Energies* **2020**, *13*, 281. [[CrossRef](#)]
28. Huang, Y.; Zhang, K.; Jiang, Z.; Song, Y.; Jiang, S.; Jia, C.; Liu, W.; Wen, M.; Xie, X.; Liu, T.; et al. A Cause Analysis of the High-Content Nitrogen and Low-Content Hydrocarbon in Shale Gas: A Case Study of the Early Cambrian in Xiuwu Basin, Yangtze Region. *Geofluids* **2019**, *2019*, 1435892. [[CrossRef](#)]
29. Chalmers, G.R.; Bustin, R.M.; Power, I.M. Characterization of gas shale pore systems by porosimetry, pycnometry, surface area, and field emission scanning electron microscopy/transmission electron microscopy image analyses: Examples from the Barnett, Woodford, Haynesville, Marcellus, and Doig units. *AAPG Bull.* **2012**, *96*, 1099–1119.
30. Loucks, R.G.; Reed, R.M.; Ruppel, S.C.; Jarvie, D.M. Morphology, Genesis, and Distribution of Nanometer-Scale Pores in Siliceous Mudstones of the Mississippian Barnett Shale. *J. Sediment. Res.* **2009**, *79*, 848–861. [[CrossRef](#)]
31. Milliken, K.L.; Rudnicki, M.; Awwiller, D.N.; Zhang, T. Organic matter-hosted pore system, Marcellus Formation (Devonian), Pennsylvania. *AAPG Bull.* **2013**, *97*, 177–200. [[CrossRef](#)]
32. Nelson, P.H. Pore-throat sizes in sandstones, tight sandstones, and shales. *AAPG Bull.* **2009**, *93*, 329–340. [[CrossRef](#)]
33. Sing, K.S.W. Reporting physisorption data for gas/solid systems with special reference to the determination of surface area and porosity (Recommendations 1984). *Pure Appl. Chem.* **1985**, *57*, 603–619. [[CrossRef](#)]
34. Liu, S.; Deng, B.; Zhong, Y.; Ran, B.; Yong, Z.; Sun, W.; Yang, D.; Jiang, L.; Ye, Y. Unique geological features of burial and superimposition of the Lower Paleozoic shale gas across the Sichuan Basin and its periphery. *Earth Sci. Front.* **2016**, *23*, 11–28. (In Chinese with English abstract)
35. Wang, Z.; Zhang, J.; Li, T.; Xie, G.; Ma, Z. Structural Analysis of the Multi-layer Detachment Folding in Eastern Sichuan Province. *Acta Geol. Sin.–Engl. Ed.* **2010**, *84*, 497–514. [[CrossRef](#)]

36. Ma, Y.; Zhong, N.; Li, D.; Pan, Z.; Cheng, L.; Liu, K. Organic matter/clay mineral intergranular pores in the Lower Cambrian Lujiaoping Shale in the north-eastern part of the upper Yangtze area, China: A possible microscopic mechanism for gas preservation. *Int. J. Coal Geol.* **2015**, *137*, 38–54. [[CrossRef](#)]
37. Liu, B.; Cheng, J.; Ye, J.; Wang, S. Shale Gas Accumulation Conditions and Gas-bearing Properties of the Lower Cambrian Shuijingtuo Formation in Well Chengtan 1, Dabashan Complex Tectonic Belt. *Acta Geol. Sin.-Engl. Ed.* **2015**, *89*, 162–163. [[CrossRef](#)]
38. Ju, Y.; Sun, Y.; Tan, J.; Bu, H.; Han, K.; Li, X.; Fang, L. The composition, pore structure characterization and deformation mechanism of coal-bearing shales from tectonically altered coalfields in eastern China. *Fuel* **2018**, *234*, 626–642. [[CrossRef](#)]
39. Zhu, H.; Ju, Y.; Qi, Y.; Huang, C.; Zhang, L. Impact of tectonism on pore type and pore structure evolution in organic-rich shale: Implications for gas storage and migration pathways in naturally deformed rocks. *Fuel* **2018**, *228*, 272–289. [[CrossRef](#)]
40. Sun, W.; Zuo, Y.; Wang, S.; Wu, Z.; Liu, H.; Zheng, L.; Lou, Y. Pore structures of shale cores in different tectonic locations in the complex tectonic region: A case study of the Niutitang Formation in Northern Guizhou, Southwest China. *J. Nat. Gas Sci. Eng.* **2020**, *80*, 103398. [[CrossRef](#)]
41. Li, X.; Zhu, H.; Zhang, K.; Li, Z.; Yu, Y.; Feng, X.; Wang, Z. Pore characteristics and pore structure deformation evolution of ductile deformed shales in the Wufeng-Longmaxi Formation, southern China. *Mar. Pet. Geol.* **2021**, *127*, 104992. [[CrossRef](#)]
42. Shi, S.; Wang, Y.; Guo, H.; Chen, C.; Deng, R. Variations in pore structure of marine shale from the same horizon of the Longmaxi Formation with changing position in a small-scale anticline: Implications for the influence of structural deformation. *Mar. Pet. Geol.* **2021**, *124*, 104837. [[CrossRef](#)]
43. Liang, M.; Wang, Z.; Zhang, Y.; Greenwell, C.H.; Li, H.; Yu, Y.; Liu, S. Experimental investigation on gas permeability in bedding shale with brittle and semi-brittle deformations under triaxial compression. *J. Pet. Sci. Eng.* **2021**, *196*, 108049. [[CrossRef](#)]
44. Han, H.; Zhong, N.; Ma, Y.; Huang, C.; Wang, Q.; Chen, S.; Lu, J. Gas storage and controlling factors in an over-mature marine shale: A case study of the Lower Cambrian Lujiaoping shale in the Dabashan arc-like thrust-fold belt, southwestern China. *J. Nat. Gas Sci. Eng.* **2016**, *33*, 839–853. [[CrossRef](#)]
45. Yue, G.Y. Tectonic Characteristics and Tectonic Evolution of Dabashan Orogenic Belt and its Foreland Basin. *J. Mineral. Petrol.* **1998**, *18*, 8–15. (In Chinese with English abstract)
46. Dong, Y.; Zhang, G.; Neubauer, F.; Liu, X.; Genser, J.; Hauzenberger, C. Tectonic evolution of the Qinling orogen, China: Review and synthesis. *J. Asian Earth Sci.* **2011**, *41*, 213–237. [[CrossRef](#)]
47. Yu, C.; Cheng, L.; Zeng, C.; Wang, S. Main controlling factor analysis on gas-bearing property of lower paleozoic shale in northeastern chongqing region. *Fault-Block Oil Gas Field* **2014**, *21*, 296–300. (In Chinese with English abstract)
48. Ma, Y.; Zhong, N.; Yao, L.; Huang, H.; Larter, S.; Jiao, W. Shale gas desorption behavior and carbon isotopic variations of gases from canister desorption of two sets of gas shales in south China. *Mar. Pet. Geol.* **2020**, *113*, 104127. [[CrossRef](#)]
49. Zhang, W. Preservation of the Shale Gas in Lower Cambrian Niutitang Formation, Southeast Chongqing. Master Thesis, China University of Petroleum, Beijing, China, 2016. (In Chinese with English abstract)
50. Pecharsky, V.; Zavalij, P. *Fundamentals of Powder Diffraction and Structural Characterization of Materials*; Kluwer Academic Publishers: New York, NY, USA, 2003.
51. Sun, J.; Xiao, X.; Cheng, P. Influence of water on shale pore heterogeneity and the implications for shale gas-bearing property—A case study of marine Longmaxi Formation shale in northern Guizhou. *Mar. Pet. Geol.* **2021**, *134*, 105379. [[CrossRef](#)]
52. Tian, H.; Pan, L.; Xiao, X.; Wilkins, R.W.T.; Meng, Z.; Huang, B. A preliminary study on the pore characterization of Lower Silurian black shales in the Chuandong Thrust Fold Belt, southwestern China using low pressure N₂ adsorption and FE-SEM methods. *Mar. Pet. Geol.* **2013**, *48*, 8–19. [[CrossRef](#)]
53. Liu, Y.; Liu, S.; Zhang, R.; Zhang, Y. The molecular model of Marcellus shale kerogen: Experimental characterization and structure reconstruction. *Int. J. Coal Geol.* **2021**, *246*, 103833. [[CrossRef](#)]
54. Chen, J.; Xu, Y.; Gai, H.; Xiao, Q.; Wen, J.; Zhou, Q.; Li, T. Understanding water accessibility and pore information of overmature marine shales using water vapor sorption. *Mar. Pet. Geol.* **2021**, *130*, 105120. [[CrossRef](#)]
55. Gu, X.; Mildner, D.F.R.; Cole, D.R.; Rother, G.; Slingerland, R.; Brantley, S.L. Quantification of Organic Porosity and Water Accessibility in Marcellus Shale Using Neutron Scattering. *Energy Fuels* **2016**, *30*, 4438–4449. [[CrossRef](#)]
56. Barrett, E.P.; Joyner, L.G.; Halenda, P.P. The Determination of Pore Volume and Area Distributions in Porous Substances. I. Computations from Nitrogen Isotherms. *J. Am. Chem. Soc.* **1951**, *73*, 373–380. [[CrossRef](#)]
57. Brunauer, S.; Emmett, P.H.; Teller, E. Adsorption of Gases in Multimolecular Layers. *J. Am. Chem. Soc.* **1938**, *60*, 309–319. [[CrossRef](#)]
58. Thommes, M.; Kaneko, K.; Neimark, A.V.; Olivier, J.P.; Rodriguez-Reinoso, F.; Rouquerol, J.; Sing, K.S.W. Physisorption of gases, with special reference to the evaluation of surface area and pore size distribution (IUPAC Technical Report). *Pure Appl. Chem.* **2015**, *87*, 1051–1069. [[CrossRef](#)]
59. Gao, P.; He, Z.; Lash, G.G.; Zhou, Q.; Xiao, X. Controls on silica enrichment of lower cambrian organic-rich shale deposits. *Mar. Pet. Geol.* **2021**, *130*, 105126. [[CrossRef](#)]
60. Luo, Q.; Zhong, N.; Dai, N.; Zhang, W. Graptolite-derived organic matter in the Wufeng-Longmaxi Formations (Upper Ordovician-Lower Silurian) of southeastern Chongqing, China: Implications for gas shale evaluation. *Int. J. Coal Geol.* **2016**, *153*, 87–98. [[CrossRef](#)]

61. Zhao, J.; Jin, Z.; Jin, Z.; Wen, X.; Geng, Y.; Yan, C. Characteristics of Biogenic Silica and Its Effect on Reservoir in Wufeng-Longmaxi Shales, Sichuan Basin. *Acta Geol. Sin.-Engl. Ed.* **2015**, *89*, 139. [[CrossRef](#)]
62. Tian, H.; Pan, L.; Zhang, T.; Xiao, X.; Meng, Z.; Huang, B. Pore characterization of organic-rich Lower Cambrian shales in Qiannan Depression of Guizhou Province, Southwestern China. *Mar. Pet. Geol.* **2015**, *62*, 28–43. [[CrossRef](#)]
63. Chalmers, G.R.L.; Ross, D.J.K.; Bustin, R.M. Geological controls on matrix permeability of Devonian Gas Shales in the Horn River and Liard basins, northeastern British Columbia, Canada. *Int. J. Coal Geol.* **2012**, *103*, 120–131. [[CrossRef](#)]
64. Loucks, R.G.; Ruppel, S.C. Mississippian Barnett Shale: Lithofacies and depositional setting of a deep-water shale-gas succession in the Fort Worth Basin, Texas. *AAPG Bull.* **2007**, *91*, 579–601. [[CrossRef](#)]
65. Mastalerz, M.; Schimmelmann, A.; Drobniak, A.; Chen, Y. Porosity of Devonian and Mississippian New Albany Shale across a maturation gradient: Insights from organic petrology, gas adsorption, and mercury intrusion. *AAPG Bull.* **2013**, *97*, 1621–1643. [[CrossRef](#)]
66. Xiao, X.; Wang, M.; Wei, Q.; Tian, H.; Pan, L.; Li, T. Evaluation of Lower Paleozoic Shale with Shale Gas Prospect in South China. *Nat. Gas Geosci.* **2015**, *26*, 1433–1445. (In Chinese with English abstract)
67. Cui, N.; Zhang, Y.; Lu, Z. Features of shale reservoir of cambrian system in Chengkou north face of northeastern Chongqing. *Sci. Technol. Eng.* **2017**, *17*, 120–127. (In Chinese with English abstract)
68. Wang, P.; Zhang, C.; Li, X.; Zhang, K.; Yuan, Y.; Zang, X.; Cui, W.; Liu, S.; Jiang, Z. Organic matter pores structure and evolution in shales based on the he ion microscopy (HIM): A case study from the Triassic Yanchang, Lower Silurian Longmaxi and Lower Cambrian Niutitang shales in China. *J. Nat. Gas Sci. Eng.* **2020**, *84*, 103682. [[CrossRef](#)]
69. Schoenherr, J.; Littke, R.; Urai, J.L.; Kukla, P.A.; Rawahi, Z. Polyphase thermal evolution in the Infra-Cambrian Ara Group (South Oman Salt Basin) as deduced by maturity of solid reservoir bitumen. *Org. Geochem.* **2007**, *38*, 1293–1318. [[CrossRef](#)]
70. Sanei, H.; Haeri-Ardakani, O.; Wood, J.M.; Curtis, M.E. Effects of nanoporosity and surface imperfections on solid bitumen reflectance (BRo) measurements in unconventional reservoirs. *Int. J. Coal Geol.* **2015**, *138*, 95–102. [[CrossRef](#)]
71. Luo, Q.; Fariborz, G.; Zhong, N.; Wang, Y.; Qiu, N.; Skovsted, C.B.; Suchý, V.; Hemmingsen Schovsbo, N.; Morga, R.; Xu, Y.; et al. Graptolites as fossil geo-thermometers and source material of hydrocarbons: An overview of four decades of progress. *Earth-Sci. Rev.* **2020**, *200*, 103000. [[CrossRef](#)]
72. Hu, H.; Hao, F.; Lin, J.; Lu, Y.; Ma, Y.; Li, Q. Organic matter-hosted pore system in the Wufeng-Longmaxi (O3w-S11) shale, Jiaoshiha area, Eastern Sichuan Basin, China. *Int. J. Coal Geol.* **2017**, *173*, 40–50. [[CrossRef](#)]
73. Liu, Z.; Guo, S.; Lv, R. Shale-gas play risk of the lower Cambrian on the Yangtze platform, South China. *AAPG Bull.* **2020**, *104*, 989–1009. [[CrossRef](#)]
74. Gai, H.; Tian, H.; Cheng, P.; He, C.; Wu, Z.; Ji, S.; Xiao, X. Characteristics of molecular nitrogen generation from overmature black shales in South China: Preliminary implications from pyrolysis experiments. *Mar. Pet. Geol.* **2020**, *120*, 104527. [[CrossRef](#)]
75. Wang, Y.; Li, X.; Chen, B.; Wu, W.; Dong, D.; Zhang, J.; Han, J.; Ma, J.; Dai, B.; Wang, H.; et al. Lower limit of thermal maturity for the carbonization of organic matter in marine shale and its exploration risk. *Pet. Explor. Dev.* **2018**, *45*, 402–411. [[CrossRef](#)]
76. Zhang, Q.; Littke, R.; Zieger, L.; Shabani, M.; Tang, X.; Zhang, J. Ediacaran, Cambrian, Ordovician, Silurian and Permian shales of the Upper Yangtze Platform, South China: Deposition, thermal maturity and shale gas potential. *Int. J. Coal Geol.* **2019**, *216*, 103281. [[CrossRef](#)]
77. Wilson, M.J.; Wilson, L.; Shaldybin, M.V. Clay mineralogy and unconventional hydrocarbon shale reservoirs in the USA. II. Implications of predominantly illitic clays on the physico-chemical properties of shales. *Earth-Sci. Rev.* **2016**, *158*, 1–8. [[CrossRef](#)]
78. Li, C.; Xiaoshi, L.; Zongxiu, W.; Mingliang, L.; Kaixun, Z.; Yuanlong, T.; Tao, T.; Li, G. Deformation characteristics of Early Paleozoic marine shale and their influence on the shale gas preservation in the eastern Sichuan-Wulingshan tectonic belt. *J. Geomech.* **2020**, *26*, 819–829. (In Chinese with English abstract)
79. Ma, Y.; Ardakani, O.; Zhong, N.; Liu, H.; Huang, H.; Larter, S.R.; Zhang, C. Possible pore structure deformation effects on the shale gas enrichment: An example from the Lower Cambrian shales of the Eastern Upper Yangtze Platform, South China. *Int. J. Coal Geol.* **2019**, *217*, 103349. [[CrossRef](#)]
80. Liu, W.; Zhang, C.; Gao, G.; Luo, C.; Wu, W.; Shi, X.; Zhang, J.; Li, W.; Deng, X.; Hu, X. Controlling factors and evolution laws of shale porosity in Longmaxi Formation, Sichuan Basin. *Acta Pet. Sin.* **2017**, *38*, 175–184. (In Chinese with English abstract)
81. Rouquerol, J.; Rouquerol, F. Methodology of Gas Adsorption. In *Adsorption by Powders and Porous Solids*, 2nd ed.; Rouquerol, F., Rouquerol, J., Sing, K.S.W., Llewellyn, P., Maurin, G., Eds.; Academic Press: Oxford, UK, 2014; pp. 57–104.
82. Groen, J.C.; Peffer, L.A.A.; Pérez-Ramírez, J. Pore size determination in modified micro- and mesoporous materials. Pitfalls and limitations in gas adsorption data analysis. *Microporous Mesoporous Mater.* **2003**, *60*, 1–17. [[CrossRef](#)]
83. Bertier, P.; Schweinar, K.; Stanjek, H.; Ghanizadeh, A.; Pipich, V. On the use and abuse of N₂ physisorption for the characterisation of the pore structure of shales. *CMS Workshop Lect.* **2016**, *21*, 151–161.
84. Liang, M.; Wang, Z.; Gao, L.; Li, C.; Li, H. Evolution of pore structure in gas shale related to structural deformation. *Fuel* **2017**, *197*, 310–319. [[CrossRef](#)]
85. Loucks, R.G.; Reed, R.M.; Ruppel, S.C.; Hammes, U. Spectrum of pore types and networks in mudrocks and a descriptive classification for matrix-related mudrock pores. *AAPG Bull.* **2012**, *96*, 1071–1098. [[CrossRef](#)]
86. Ji, L.; Ma, X.; Xia, Y.; Qiu, J. Relationship between Methane Adsorption Capacity of Clay Minerals and Micropore Volume. *Nat. Gas Geosci.* **2014**, *25*, 141–152. (In Chinese with English abstract)

87. Ji, L.; Qiu, J.; Xia, Y.; Zhang, T. Micro-pore characteristics and methane adsorption properties of common clay minerals by electron microscope scanning. *Acta Pet. Sin.* **2012**, *33*, 249–256. (In Chinese with English abstract)
88. Li, Q.; Cai, Y.; Hu, H. Characteristics of nano-pore structure of clay minerals in shale and its effects on methane adsorption capacity. *J. China Coal Soc.* **2017**, *42*, 2414–2419. (In Chinese with English abstract)
89. Liu, L.; Tang, S.; Xi, Z. Total Organic Carbon Enrichment and Its Impact on Pore Characteristics: A Case Study from the Niutitang Formation Shales in Northern Guizhou. *Energies* **2019**, *12*, 1480. [[CrossRef](#)]
90. Kuila, U.; Prasad, M. Application of nitrogen gas-adsorption technique for characterization of pore structure of mudrocks. *Lead. Edge* **2013**, *32*, 1478–1485. [[CrossRef](#)]
91. Cao, T.; Song, Z.; Wang, S.; Xia, J. A comparative study of the specific surface area and pore structure of different shales and their kerogens. *Sci. China Earth Sci.* **2015**, *58*, 510–522. [[CrossRef](#)]
92. Chen, Y.; Qin, Y.; Wei, C.; Huang, L.; Shi, Q.; Wu, C.; Zhang, X. Porosity changes in progressively pulverized anthracite subsamples: Implications for the study of closed pore distribution in coals. *Fuel* **2018**, *225*, 612–622. [[CrossRef](#)]
93. Etminan, S.R.; Javadpour, F.; Maini, B.B.; Chen, Z. Measurement of gas storage processes in shale and of the molecular diffusion coefficient in kerogen. *Int. J. Coal Geol.* **2014**, *123*, 10–19. [[CrossRef](#)]
94. Chen, M.; Kang, Y.; Zhang, T.; You, L.; Li, X.; Chen, Z.; Wu, K.; Yang, B. Methane diffusion in shales with multiple pore sizes at supercritical conditions. *Chem. Eng. J.* **2018**, *334*, 1455–1465. [[CrossRef](#)]
95. Wu, K.; Li, X.; Guo, C.; Wang, C.; Chen, Z. A Unified Model for Gas Transfer in Nanopores of Shale-Gas Reservoirs: Coupling Pore Diffusion and Surface Diffusion. *SPE J.* **2016**, *21*, 1583–1611. [[CrossRef](#)]
96. Mi, L.; Jiang, H.; Li, J. The impact of diffusion type on multiscale discrete fracture model numerical simulation for shale gas. *J. Nat. Gas Sci. Eng.* **2014**, *20*, 74–81. [[CrossRef](#)]
97. Zou, Y.; Wang, G.; Lu, L.; Zhu, H.; Liu, G.; Yuan, Y.; Yang, H.; Jin, Z. Simulation experiment and mathematical model analysis for shale gas diffusion in nano-scale pores. *Pet. Geol. Exp.* **2021**, *43*, 844–854. (In Chinese with English abstract)